Institute for Space Nuclear Power Studies
Department of Chemical and Nuclear Engineering
The University of New Mexico
Albuquerque, New Mexico 87131

NATURAL CIRCULATION DECAY HEAT REMOVAL FROM AN SP-100, 550 kWe POWER SYSTEM FOR A LUNAR OUTPOST

Mohamed S. El-Genk and Huimin Xue

Final Report No. UNM-ISNPS-4-92

June 1992

TABLE OF CONTENTS

List of Figures

I

List of Tables

III

ACKNOWLEDGMENTS

IV

NOMENCLATURE

a	Width of the DHE duct, m,
b	Height of DHE duct, m,
A	Area, m^2.
A_{hp}	Cross section flow area of vapor in heat pipe, m^2.
C	Specific heat, J/kg K,
D	Fuel pin, or pipe diameter, m,
D_e	Equivalent hydraulic diameter, m,
f	Friction coefficient,
F	Radiation view factor,
g	Acceleration of gravity, m/sec^2,
h	Heat transfer coefficient, W/m^2 K, latent heat, J/kg,
H	Height of reactor, m
h_{fg}	Latent heat of vaporization, kJ/kg.
k	Thermal conductivity, W/m K,
L	Length of the coolant flow path in DHRL, m.
$\dot{m}$	Coolant mass flow rate, kg/s,
Nu	Nusselt number, (h De/k),
Nu_s	Slug Nusselt number, equation (24),
p	Pressure, MPa,
P	Pressure, MPa, or power, W, or pitch distance, m,
P_e	Peclet number (Re. Pr),
Pr	Prandtl number, $(C_p \mu/k)$,
P/D	Pitch-to-diameter ratio,
q'''	Volumetric decay heat , W/m^3,
q_l	Linear power, W/m,
r	Radial coordinate, m,
R	Radius of fuel pin, m,
Re	Reynolds number , $(\rho v D_e/\mu)$,
s	Diameter of the wrap wire, m,
t	Time, s,
T	Temperature , K,

U	Overall heat transfer coefficient, Equation.(22),
v	Flow velocity, m/s,
z	Distance from the entrance of reactor core, m,
Z	Dimensionless distance from the entrance of reactor core, m.

Subscripts

a	Ambient,
b	Coolant bulk,
c	Lithium coolant, cladding,
eff	Effective
f	Flow, fuel,
g	Fuel-cladding gap,
h	Convection heat transfer, heat transfer,
L	Liquid coolant, DHRL,
hp	Heat pipe,
i	Inner surface,
m	Log-mean, lunar surface,
o	Initial,
r	Radiation,
rej	Rejection,
loss	Losses,
sonic	At heat pipe sonic limit,
s	Cross-section,
v	Saturated vapor,
w	Wall.

Superscripts

Core	SP-100 reactor core
Pipe	DHRL pipes

Greek Letters

δ	Thickness, m,
ε	Emissivity,
σ	Stefan-Boltzmann constant $(5.669 \times 10^{-8} \ W/m^2 \ K^4)$
μ	Dynamic viscosity, kg/m s,
ρ	Density, kg/m^3.

1. INTRODUCTION

A permanent outpost on the moon is being considered by NASA for the early part of the next century. The lunar reference mission objectives are prioritized as follows: (1) to establish a lunar outpost with a long-term manned presence, (2) to gain experience in working on planetary surfaces, (3) to conduct scientific and manufacturing resources, and (4) to develop crew planning capabilities. The operation concept for the lunar outposts provide for the eventual decentralization of operation control, whereby planning, monitoring and controlling functions will be shifted from being earth-based to being shared by earth and the outpost.[1,2] The power requirements and decentralization of operation control will evolve within mission's successive phases. These phases are precursor/emplacement, consolidation and utilization/demonstration. While the power requirements for the precursor/emplacement phase are in the tens of kilowatts electric, they could grow to the hundreds of kilowatts electric in the utilization/demonstration phase.

Operation analysis of the manpower, machine resources and power requirements through the year 2,013 for the lunar program was conducted.[1,2] The stationary power systems for the lunar outpost will be designed to meet the evolutionary growth in power demand ranging from the tens to hundreds of kilowatts electric. As the power demand increases for a constructible habitat, an SP-100 reactor, coupled to a number of dynamic energy conversion engines, is emplaced to supply 550 kW_e. This power level has been selected based on the NASA Space Exploration Initiative 90-day study.[1]

A recent study suggested that an SP-100, 550-kWe power system, with four Stirling or Brayton engines (three operating and one standby) would be optimum for reliability consideration.[4] In addition to system reliability and redundancy, it is important that the integrity of the nuclear reactor core be maintained during a loss-of-flow accident. As a result, the power system is designed with passive means for the removal of decay heat by natural circulation from the reactor core after shutdown. The decay heat removal loop of the system is equipped with a separate heat exchanger and a heat rejection radiator on the lunar surface. More

details on the power system description and operation are included in the next section.

This research investigated the decay heat removal from the SP-100 reactor core of a 550-kWe power system for a lunar outpost by natural circulation of lithium coolant. A transient model that simulates the decay heat removal loop (DHRL) of the power system was developed and used to assess the system's decay heat removal capability. The effects of the surface area of the decay heat rejection radiator, the dimensions of the decay heat exchanger (DHE) flow duct, the elevation of the DHE, and the diameter of the rise and down pipes in the DHRL on the decay heat removal capability were examined. Also, to determine the applicability of test results at earth gravity to actual system performance on the lunar surface, the effect of the gravity constant (1g and 1/6g) on the thermal behavior of the system after shutdown was investigated.

The following section presents background information on the design and the materials used for the SP-100 nuclear reactor and a detailed description of the SP-100 fuel element. Section 3 gives a detailed description and discussion of the NASA SP-100, 550-kWe power system for a lunar outpost. Section 4 presents the mathematical formulations, governing equations, and method of solutions for each of the component's model as well as for the fully integrated decay heat removal loop model. Section 5 presents the transient results on the decay heat removal capability of the DHRL with emphasis on both time and spatial changes of the coolant temperature within the DHRL. In this section, the results of the parametric analyses, investigating the effects of DHE dimension and elevation, decay heat radiator area, guard vessel heat pipe diameter, external pipe diameter and gravity on the passive removal of decay heat in the SP-100, 550-kWe power system, are also presented and discussed. In section 6, a summary of the important results is given and conclusions are stated. More information on the mathematical formulations is given in the appendices at the end of the report.

2. BACKGROUND

The SP-100 space nuclear power system technology is being developed under a joint program between the Department of Energy (DOE), National Aeronautics and Space Administration (NASA), and the Department of Defense (DOD) to support future space missions with electric power requirements in the tens to hundreds of kilowatt electric.[3] The base 100-kWe power system design for a space mission to be developed in the earth's orbit utilizes SiGe thermoelectric (TE) generators to partially convert the reactor thermal power into electrical power with an efficiency of about 6 percent. To enhance the electrical power output of the SP-100 system to supply surface power for a lunar base, NASA will replace the TE converter with a dynamic system, such as free-piston Stirling (FPS) or Closed Brayton Cycle (CBC) engines, with an efficiency that could be more than three times larger. Therefore the SP-100 nuclear reactor technology and design can be used, while the electrical output can be increased to more than 500 kWe by such a power system.

The SP-100 nuclear assembly includes the reactor, shield and control systems. The SP-100 is a fast spectrum reactor cooled by pumped liquid lithium. The critical components of the reactor are: (1) fuel and cladding, (2) honeycomb structure, (3) reflector supports, (4) safety rod thimbles, (5) grid for pin support, (6) reactor vessel, (7) core support structure, and, (8) piping that interfaces with the primary heat transport subsystem. Figure (1) displays these components in the flight configuration and the core layout. The reactor core, in a triangular arrangement, is enclosed in a niobium refractory alloy known as a PWC-11 vessel. This alloy is niobium - 1% zirconium with 1000 ppm of carbon added to improve its high temperature creep strength.

The fuel pins are arranged in the reactor in approximately 61 hexagon assembly groups. Each group is housed with one of the hexagonal cells with the honeycomb structure of the core. This honeycomb structure prevents unacceptable fuel pin blowing and fluid cross flowing within the reactor core. A shadow shield (LiH/W) that attenuates both neutrons and gammas is employed to protect the spacecraft electronics from the radiation emitted for the reactor. The same reactor design and shadow shield assembly will be used in the 550-kWe

3
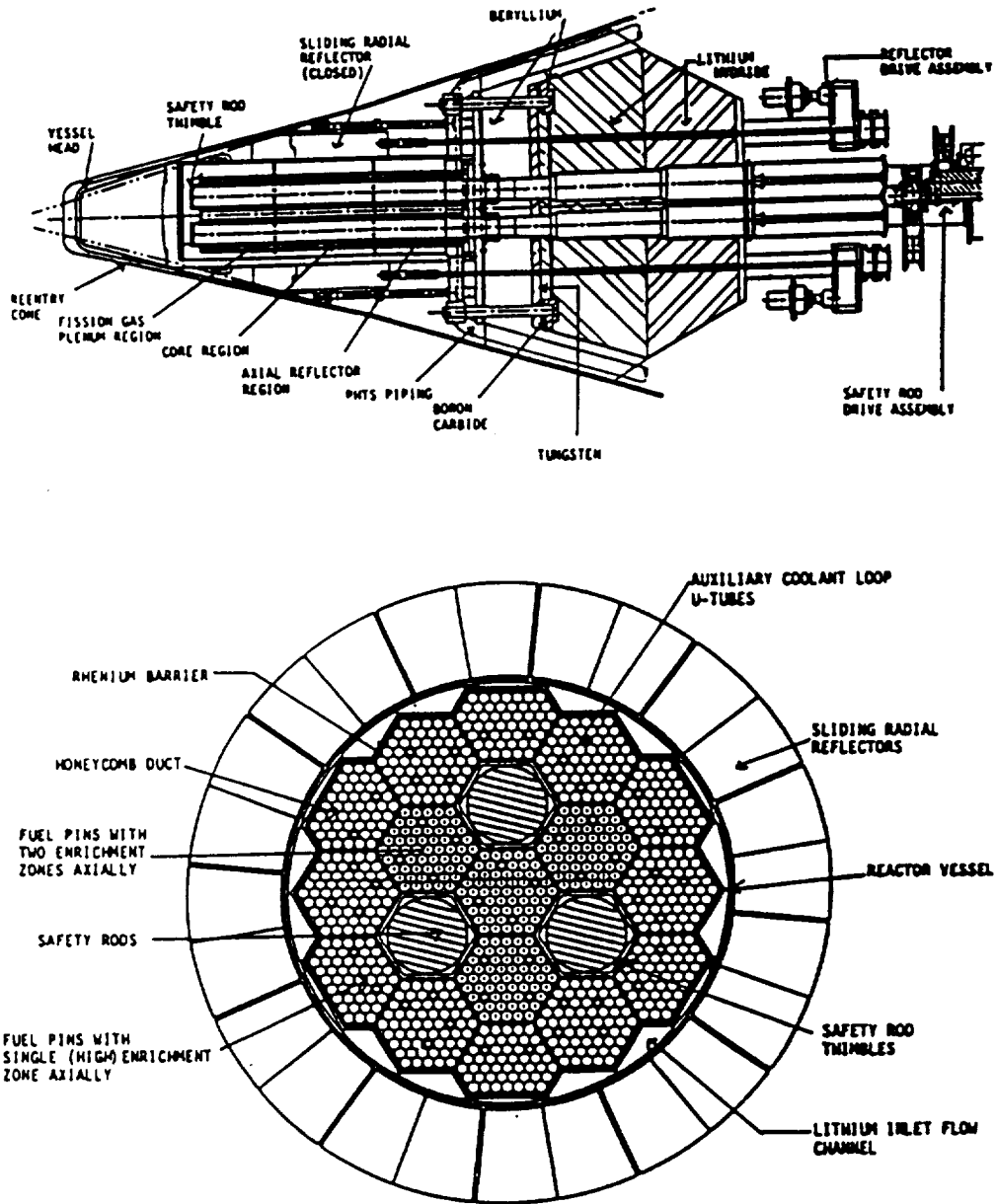
Fig. 1.　　SP-100 Reactor Subsystem Components.

power system for a lunar outpost. Given a reactor thermal power of approximately 2.3 MW_t and nominal conversion efficiency of the dynamic conversion engines of 23%-25%, a net electrical power output of 529-575 kW_e can be obtained.

The fuel pin structure is detailed in Fig. (2). Because uranium nitrite (UN) has high thermal conductivity, high uranium density and low fission gas release/swelling, the fuel pins in the SP-100 utilize it as fuel material. The UN fuel region in the fuel pin is bounded by Berylium Oxide neutron reflector materials on both ends. A plenum is located at the top of the upper reflector to accommodate the fission gasses released from the fuel. A rhenium (Re) liner is placed between the helium filled fuel gap and the Nb-1% Zr cladding. This Re liner is used to enhance flooding subcriticality and high temperature strength and to provide a chemical barrier. On the outer surface of the cladding, a wire wrap is attached to maintain proper space among fuel pins and to enhance heat transfer from the fuel pin to the coolant during normal operation. The fuel pins are arranged in a triangular lattice with a pitch-to-diameter ratio of 1.07.

CROSS SECTION

UN FUEL PELLET

HELIUM FILLED GAS GAP

Re LINER

Nb-1Zr CLADDING

Nb-1Zr CLADDING
• AVAILABLE
• FABRICABLE
• SUCCESSFUL FUEL TESTS
• COMPATIBLE WITH Li

PLENUM

Re LINER
• CHEMICAL BARRIER
• DUCTILE
• ENHANCED FLOODING SUBCRITICALITY
• HIGH TEMPERATURE STRENGTH

FUEL

UN FUEL
• HIGH THERMAL CONDUCTIVITY
• CHEMICAL COMPATIBILITY
• HIGH URANIUM DENSITY
• LOW FISSION GAS RELEASE/ SWELLING

BeO
• NEUTRON REFLECTOR

AFT AXIAL REFLECTOR

Fig. 2   Fuel Pin Configuration.

3. SP-100, 550-kW$_e$ POWER SYSTEM FOR A LUNAR OUTPOST

The SP-100, 550-kWe nuclear power system for a lunar outpost is currently being developed by Rockwell International Corporation for the National Aeronautical and Space Administration (NASA).[4] The power system employs an SP-100 nuclear reactor cooled with liquid lithium, which is coupled to four dynamic energy conversion engines (either a Brayton or Stirling power conversion subsystem). Figure (3) shows a pictorial view of the SP-100, 550 kWe power system for a lunar outpost. The whole system is emplaced inside a cylindrical, excavated cavity in the lunar regolith. A cavity liner (Guard Vessel) is provided as an integral part of the system. In the primary loop, the lithium coolant from the core is circulated by an electromagnetic (EM) pump, through the primary side of an intermediate heat exchanger, then returned to the reactor core. An expansion tank with a free lithium surface is located at the high point of the primary loop. This allows for expansion of the lithium as it heats up and for collection of the helium gas formed by the neutron interaction with the lithium. The primary loop is thermally coupled, via the intermediate heat exchanger, to either liquid lithium (for Stirling System) or He-Xe gas (for Brayton System) in four secondary loops. Each is equipped with a pump and a dynamic energy conversion (Stirling/Brayton) engine. The intermediate heat exchanger isolates the power conversion heat transfer fluid from the reactor coolant, thereby reducing the possibility of fission product contamination of any component located at the lunar surface. The primary loop EM pump is a flat linear induction pump with redundant starters and power supplies.[4]

As shown in Fig. (3), the guard vessel fits closely around the reactor and the primary coolant loop to ensure that the reactor core is always covered with lithium coolant in the event of a small leakage happening in the primary loop or a partial/total loss of flow. The entire power system, with the exception of the radiators, is emplaced in a cylindrical, excavated cavity in the lunar regolith. The primary coolant loop, the radiation shadow shield and the SP-100 reactor are located at the bottom of the cavity and the secondary loop components are placed at the top of the cavity. The cavity is lined with a stainless-steel guard vessel, which is an integral part of the system and is cooled on its outer surface by heat pipes. The guard vessel heat pipes are integrated with those of the dedicated radiators on the lunar surface for auxiliary and decay heat removal.

7
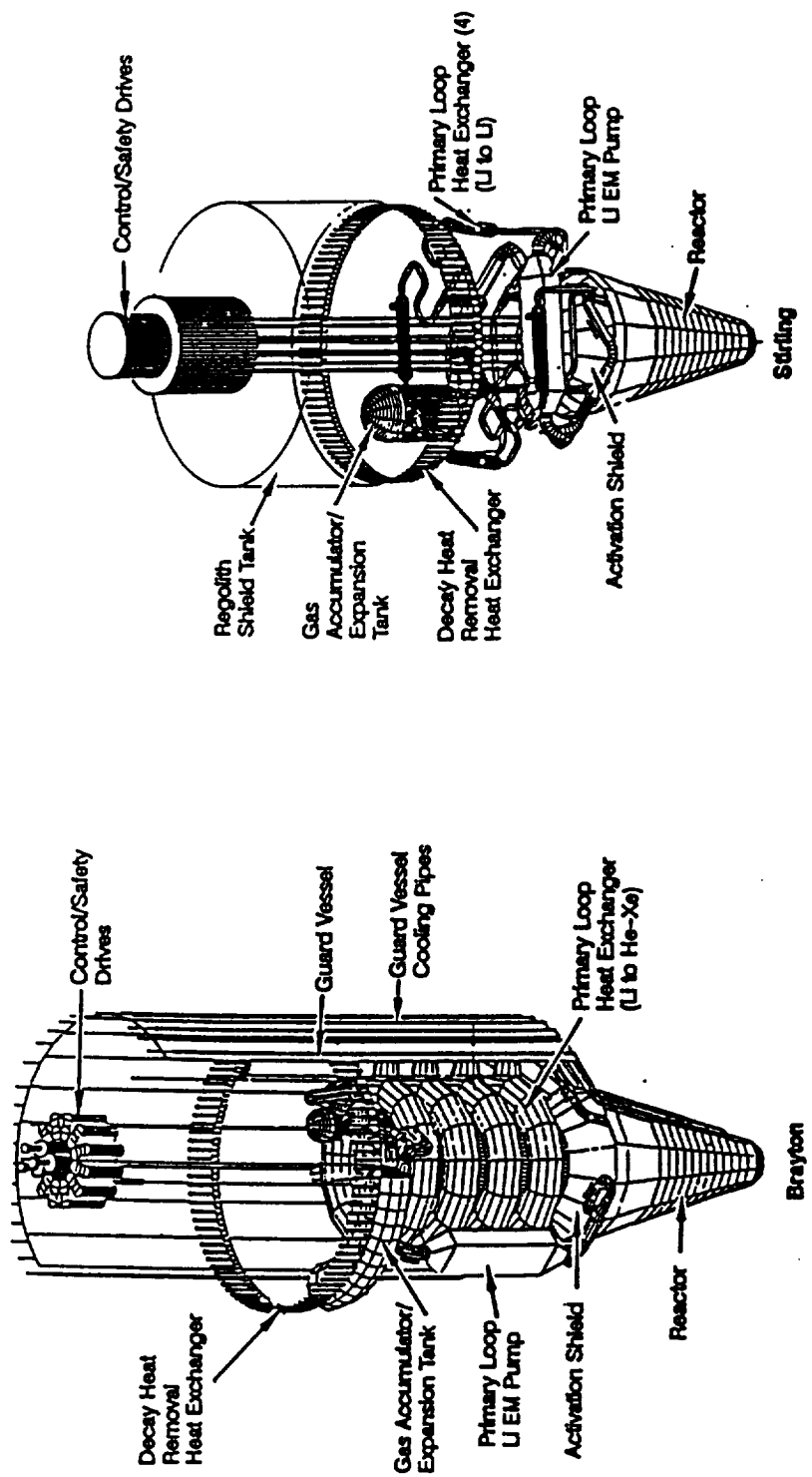
Fig. 3   A Pictorial View of an SP-100,550 kWe Power System for a Lunar
Outpost (courtesy of Rockwell International Corp.).

8

These decay heat radiators are located between the main radiator panels. In addition to the obvious structural and integrational advantages, the guard vessel is used to transport the heat losses from the reactor/primary cooling system and the energy deposited in the vessel structure by neutrons and gammas during nominal power operation, as well as the reactor decay heat after shutdown.

The flow schematic and state points for the Brayton system are shown in Fig. (4). A single primary Li loop transports heat from the reactor to the Brayton primary heat exchanger. The Brayton cycle uses an He-Xe gas mixture as the working fluid. Heat is rejected from the cycle through a NaK heat rejection loop. Each Brayton loop is cross-coupled to each of four radiator panels so that if a power conversion failure occurs, there is no loss of radiator area. The NaK loop is also used to cool the Brayton alternator.

The flow schematic and state points for the Stirling system are shown in Fig. (5). The primary and secondary Li loops are used to transport heat to the Stirling engine heater. Helium is used as the working fluid for the Stirling cycle. Heat is rejected from the Stirling cooler through a Nak heat rejection loop, which is also used to cool the alternator. As with the Brayton system, the heat rejection loops in the Stirling system are cross-coupled to each radiator panel.

Figure (6) presents a line diagram of the overall deployed arrangement for the Stirling/Brayton system with the exception the guard vessel and decay heat radiators. As shown in Fig. (6), the four conversion engines are coupled in parallel to four separate radiator panels on the lunar surface. Therefore, a failure of one of the engines or a loss-of-flow in one of the secondary loops will not affect the operation of the other three engines. In this case, the heat rejection of the system will be handled by the four radiator panels, but only three engines would supply the 550 kWe needed for the lunar outpost operation.

As Figs. (3) and (6) show, the decay heat exchanger (DHE) is an integral part of the primary coolant loop. The DHE is hydrodynamically coupled to the primary coolant loop in the hot line and in the return line via a venturi. The DHE has a rectangular flow duct and, as shown in Fig. (3), it is equipped with small sodium heat pipes to increase its effective surface area. There are about 100

State Point	Fluid	Temperature (K)	Pressure (kPa)
1	Li	1355	—
2	Li	1276	—
3	He-Xe	1300	1,280
4	He-Xe	1041	680
5	He-Xe	640	680
6	He-Xe	406	675
7	He-Xe	556	1,340
8	He-Xe	957	1,330
9	NaK	629	—
10	NaK	395	—
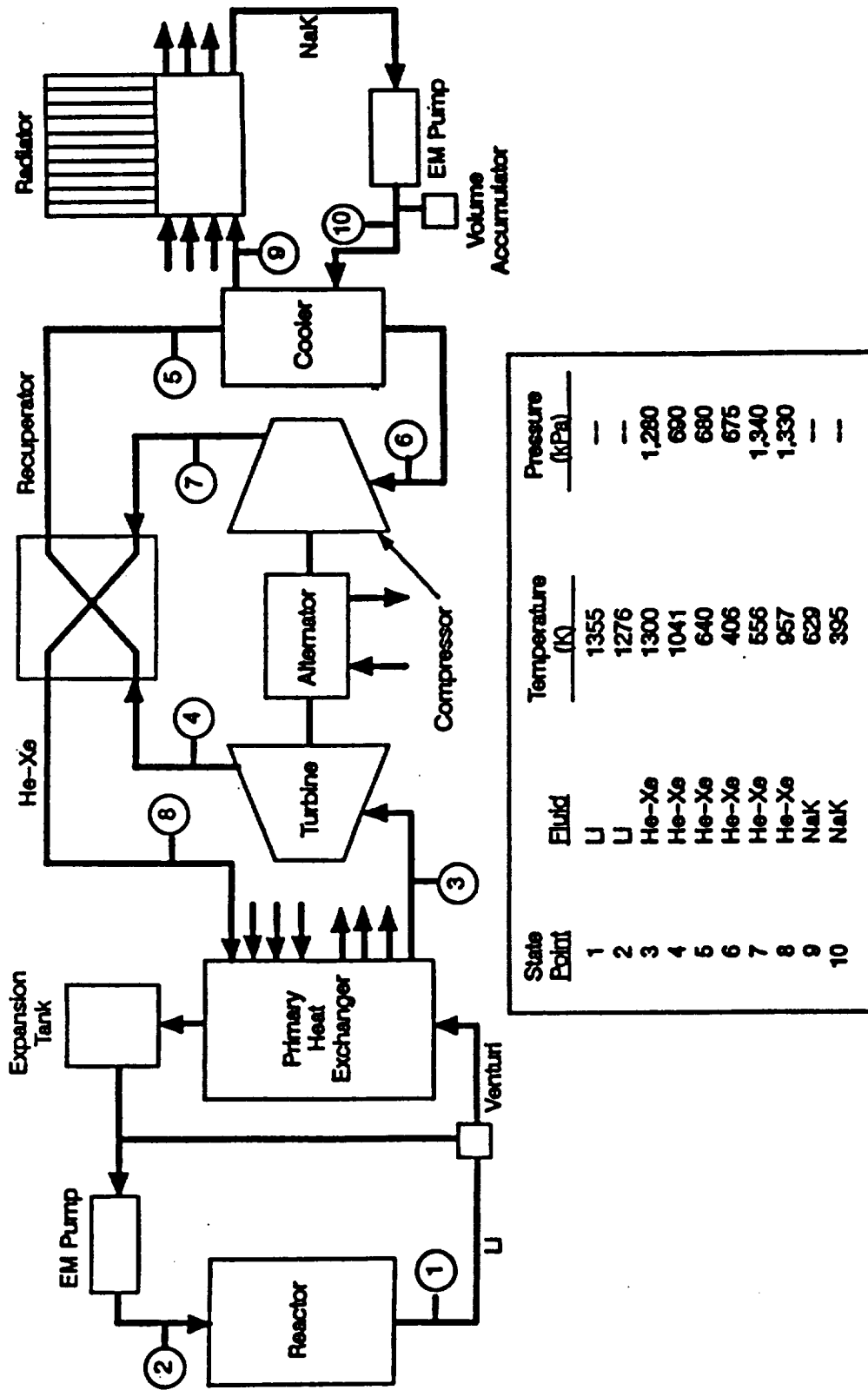
Fig. 4   SP-100,550 kWe Brayton Flow Schematic and State Point.

State Point	Fluid	Temperature (K)
1	Li	1355
2	Li	1276
3	Li	1304
4	Li	1225
5	NaK	625
6	NaK	552
T_h	—	1265
T_c	—	602
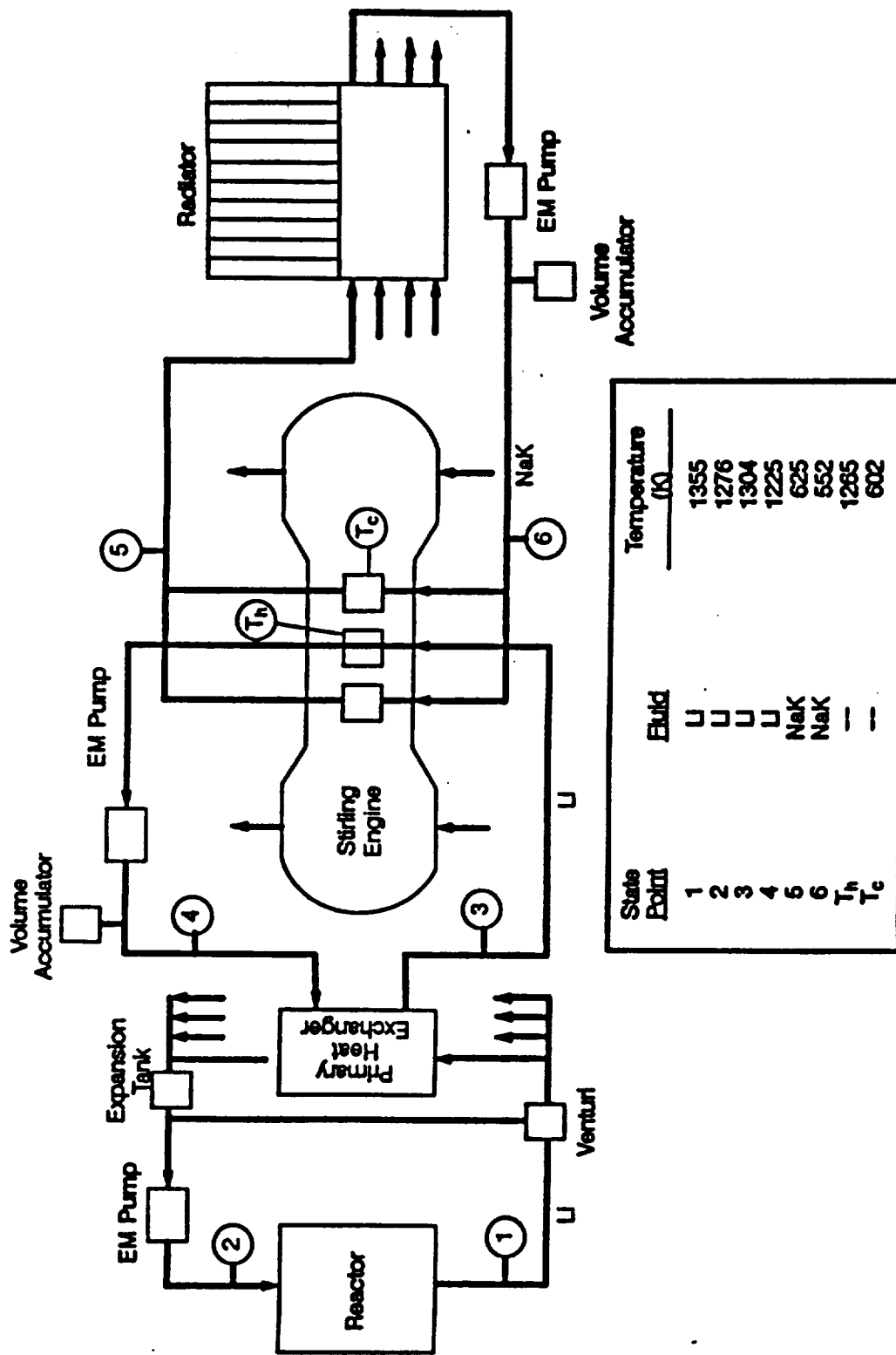
Fig. 5   SP-100,550 kWe Stirling Flow Schematic and State Point.
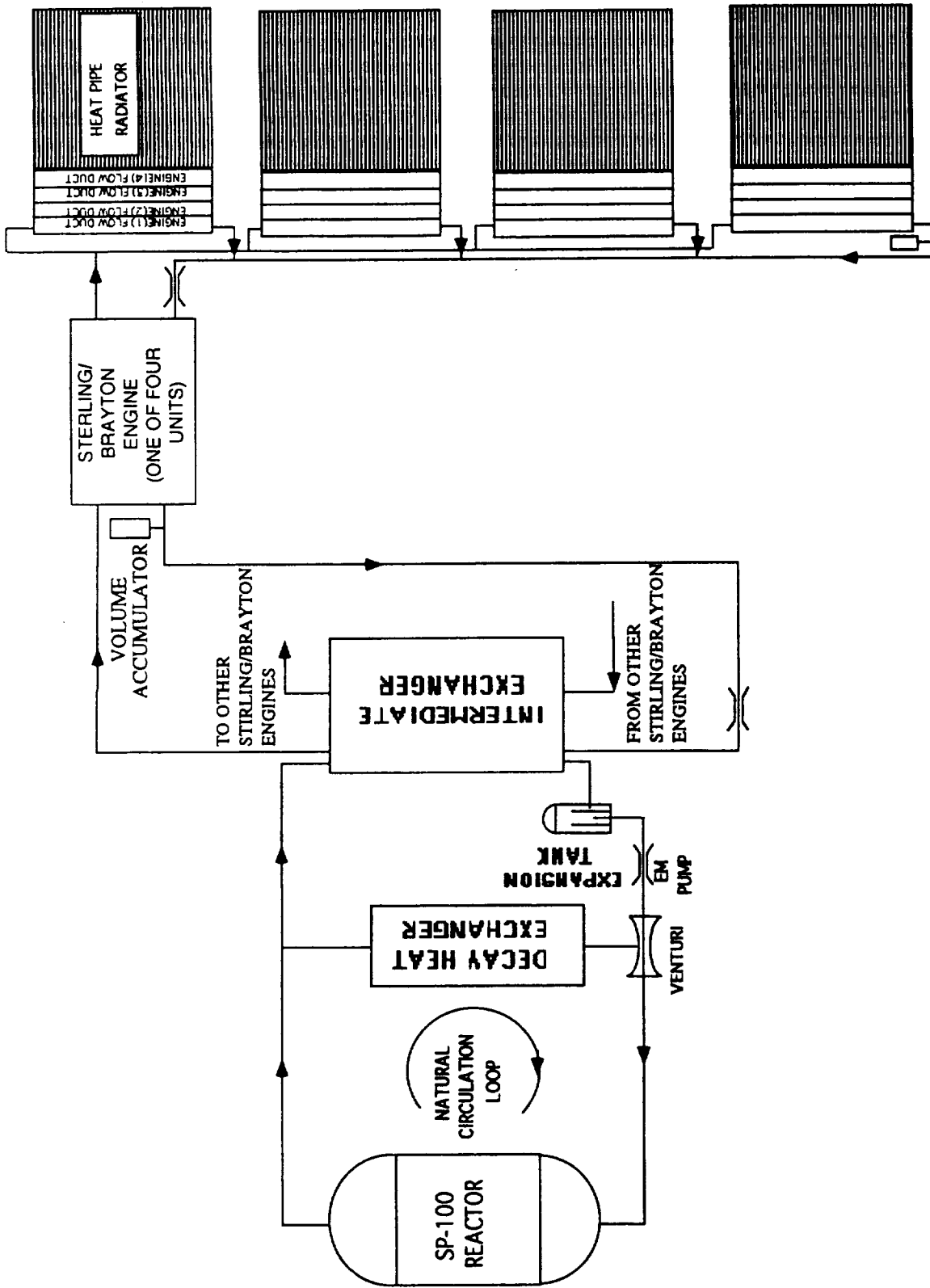
Fig. 6   A Line Diagram of an SP-100,550 kWe Power System for a Lunar
Outpost.

such sodium heat pipes measuring 30 cm in length and 2.75 cm in diameter in the current design.[22]

Figure (7) presents a schematic diagram of the DHRL. During normal power operation, the venturi in the primary coolant loop equalizes the pressure drop across the DHE hence net flow occurs through the decay heat exchanger is zero. However, following a hypothetical Loss-of-Flow Accident (LOFA), forced flow through the venturi drops to zero, hence allowing natural circulation of lithium coolant through the DHE duct under the effect of the difference in coolant densities in the rise and down pipes of the DHRL (see Fig. (7)). The heat rejection from the DHE is accomplished by radiation to the inside wall of the guard vessel, where heat is transported by the guard vessel heat pipes to the decay heat radiators on the lunar surface. These radiators are separated from those used for heat rejection from the energy conversion engines during normal full power operation of the power system. All primary loop components are electrically trace heated to provide for controlled Li thaw during start-up.

To investigate the thermal behavior of the SP-100, 550-kWe power system for a lunar outpost after reactor shutdown, an integrated model of the system's decay heat removal loop by natural circulation of primary Lithium coolant has been developed. This integrated model is described in detail in the following section.
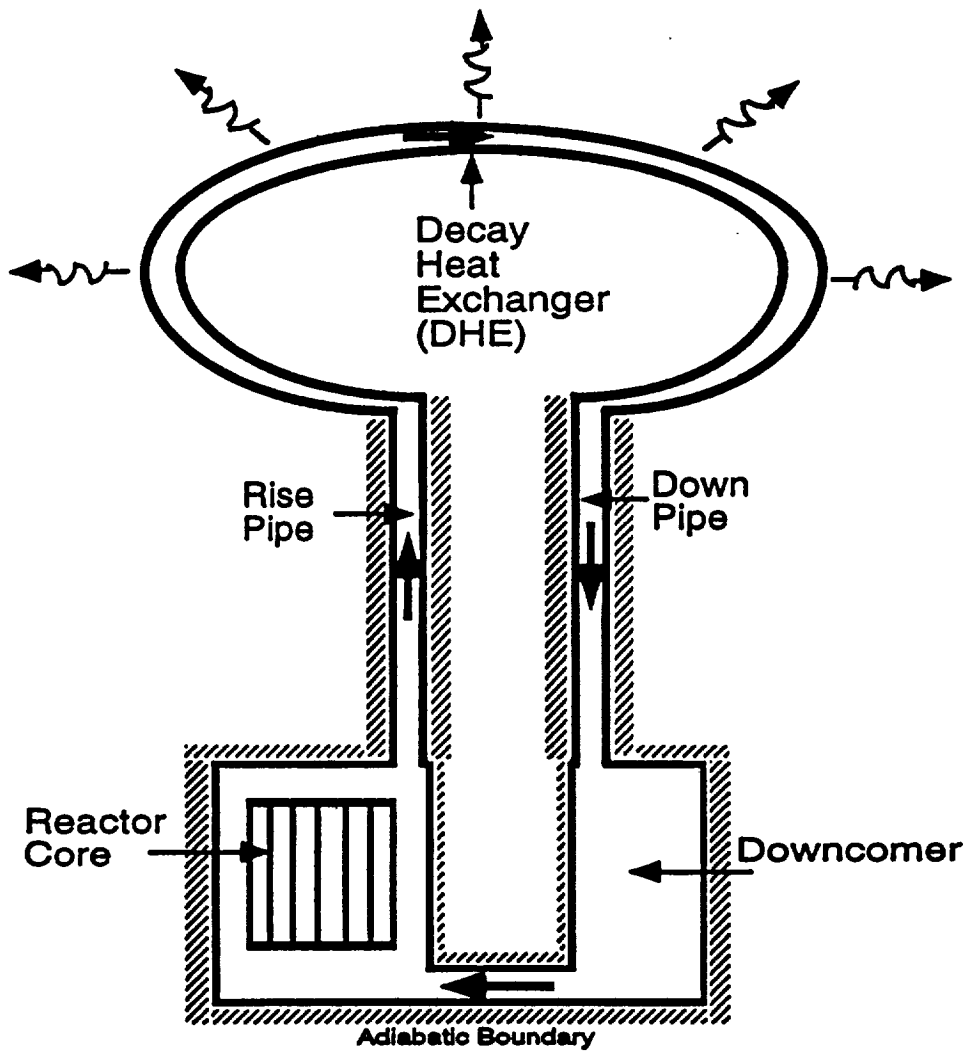
Fig. 7   A Schematic Diagram of Decay Heat Removal Loop.

4. MODEL DESCRIPTION

The integrated decay heat removal model of the SP-100, 550-kWe system developed herein consists of three coupled sub-models: (a) two-dimensional transient thermal model of the fuel pin, (b) transient natural circulation thermal-hydraulic model of the DHRL, and (c) heat rejection model for the DHE/guard vessel heat pipes. The properties of the lithium coolant and those of the fuel, cladding, and structural materials are taken to be temperature dependent. As indicated earlier, the decay heat exchanger is radiatively coupled to the inside surface of the guard vessel. The radiation view factor between the DHE and the guard vessel is calculated as a function of the dimensions of both the DHE and the guard vessel.[6] (In Appendix A, an analysis is performed to estimate the radiation view factor between the DHE and guard vessel.) However, the effective surface emissivity for the DHE wall and the inside surface of the guard vessel are assumed constant during the analysis (see Table 1). Fig. (8) shows a block diagram of the DHRL model.

4.1 Two-Dimensional Transient Thermal Model of Fuel Pin

The fuel pin model calculates the radial and axial temperature distributions inside the fuel pin as functions of heat generation in the fuel (fission power or decay power), coolant mass flow rate, and coolant temperature in the reactor core. Although the two-dimensional heat transfer equation can be used for this purpose, this can be simplified by neglecting the axial heat conduction. This assumption is justified by the negligible axial heat conduction due to the long length of the fuel pin compared to its radius and high thermal conductivity of the UN fuel. In this model, the fuel pin is discretized into small axial segments (see Fig. (9)), and in each segment the radial transient heat conduction equation is solved while the axial heat conduction between segments is neglected. The axial temperature distribution in the fuel pin is obtained by thermal-hydraulically coupling the different axial segments.

15
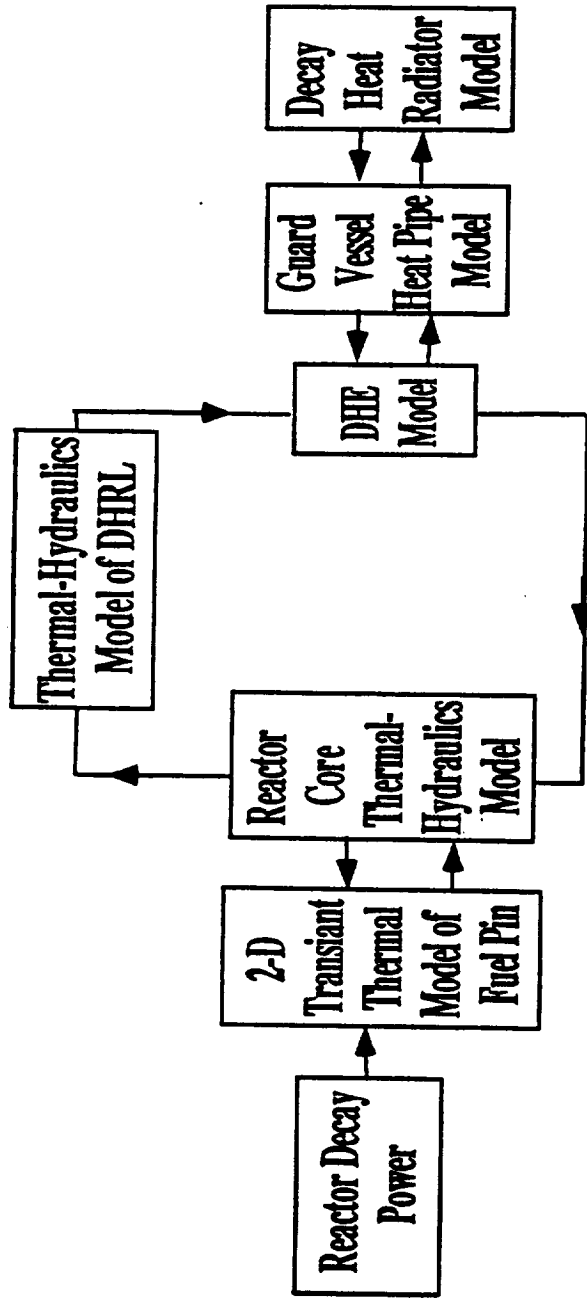
Fig. 8   Block Diagram of the Decay Heat Removal Loop Model.
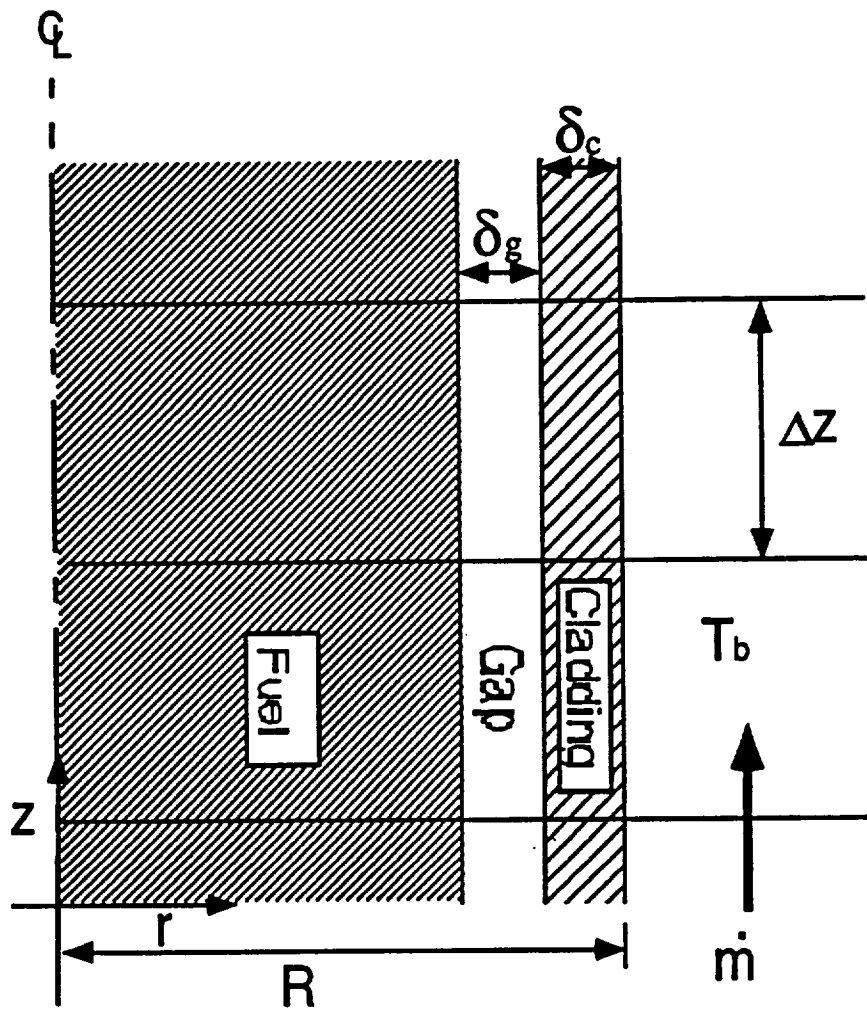
Fig. 9   A Schematic Diagram of the 2-D Fuel Pin Thermal Model.

4.1.1 Governing Equations

In each axial segment in the fuel pin, only the radial heat conduction is considered. The transient radial heat conduction equation is:

$$\rho_f C_f \frac{\partial T(r,t)}{\partial t} = \frac{1}{r} \frac{\partial}{\partial r} \left(k_f r \frac{\partial T(r,t)}{\partial r} \right) + q'''(r,t) \quad . \tag{1}$$

In the cladding and the fuel-cladding gap, the second term on the right hand side of Eq. (1), the volumetric heat source, is zero.

The heat source term $q'''(r,t)$ in Eq. (1) is the decay heat inside the fuel region in our decay heat removal calculation. This decay power is the function of the fission power level and reactor operation time before shutdown and fuel material composition. In our analyses, the decay heat generation in the fuel region is calculated using the decay heat curves recommended by Marr and Bunch.[10] Fig. (10) presents these decay heat curves for fast spectrum reactors as a function of time after shutdown. These curves are plotted using a long reactor operation time before shutdown (> 6 months).

The initial and boundary conditions for the fuel pin model are:

$$T(r,0) = T_o(r), \left(\frac{\partial T(0,t)}{\partial r} \right) = 0 \quad , \tag{2a}$$

$$k_f \left(\frac{\partial T(R,t)}{\partial r} \right) = h \left(T(R,t) - T_b(t) \right) \quad . \tag{2b}$$

In Eq. (2b), the heat transfer coefficient between the lithium coolant and the cladding, h, is calculated using a natural convection heat transfer correlation for triangular lattices bundles:[8]

$$Nu = 24.0 \left((A_f / A_h)^{1.8} . Pe \right)^{0.6} \quad , \tag{3}$$

18
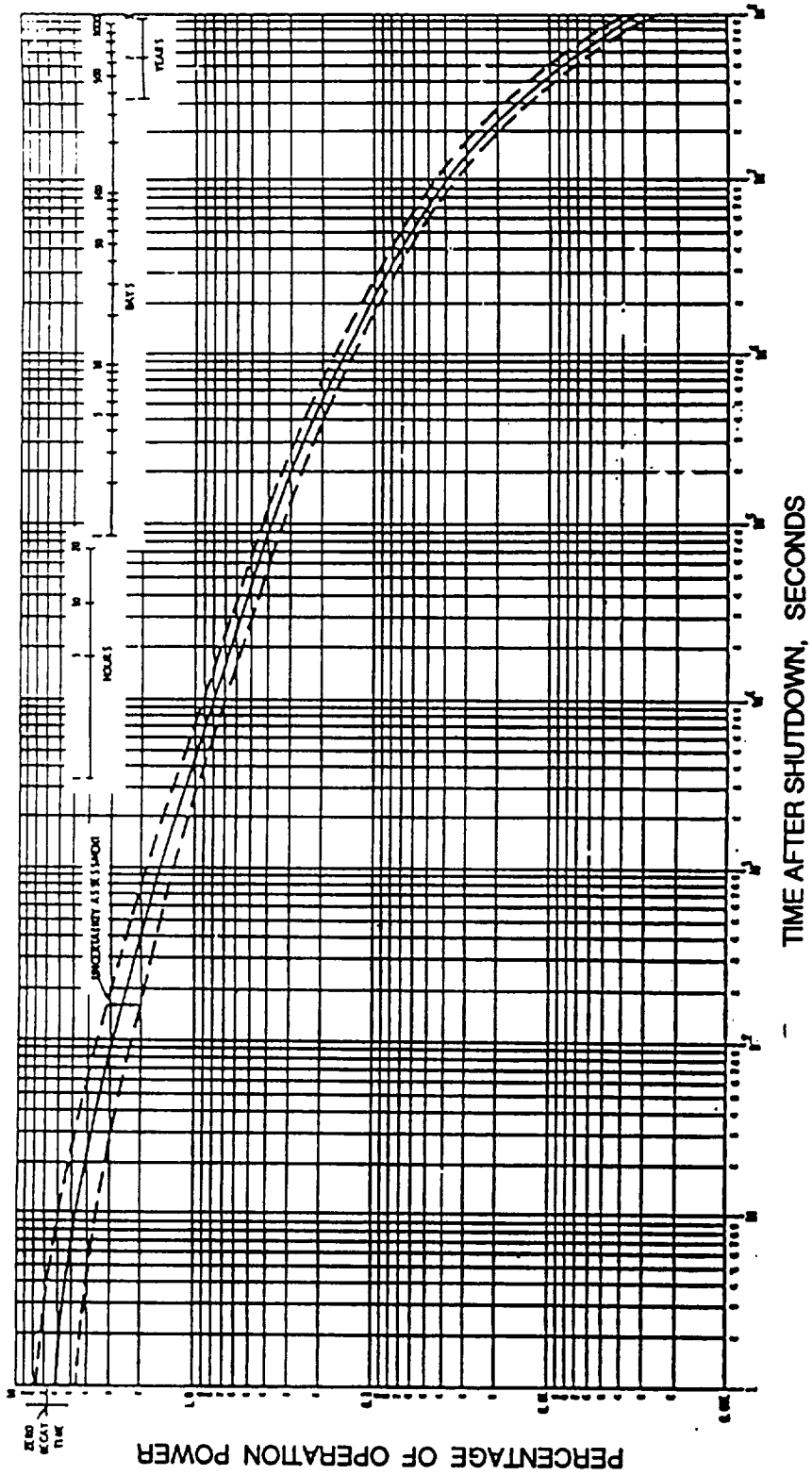
Fig. 10   Decay Heat Curves for Fast Spectrum Reactors.

19

where A_f and A_h are the flow area and the heat transfer area in the core respectively.

In the gap between fuel and cladding, the gap thermal conductance is calculated using either a closed or an open gap model, which allows for fission gas release into the gap during reactor operation.[7] For the open gap case, the gap conductance is given as:

$$h = h_k + h_r \ . \tag{4}$$

In this equation, h_k is the contribution of thermal conduction through the gas mixture inside the gap and h_r is the thermal radiation contribution of between the surface of the fuel and the cladding.

For the closed gap, the overall gap conductance is taken as the sum of conduction and radiation contribution through the gas entrapped between the fuel and cladding inner surface, h_k and h_r, and the solid-solid conduction at the contact point, h_s:

$$h = h_k + h_r + h_s \ . \tag{5}$$

The thermal conduction through the gas gap is given as:[18]

$$h_k = \frac{k_g}{(\delta_f + \delta_c) + G + (g_f + g_c)} \ , \tag{6}$$

where δ is the surface roughness, g is the jump distance and G is the gap thickness. The subscripts f and c represent the fuel and cladding respectively. In Eq. (6), the thermal conductivity of the gas mixture, k_g, is calculated as:

$$k_g = (k_1)^{\chi_1}(k_2)^{\chi_2}(k_3)^{\chi_3} \ , \tag{7a}$$

where

$$k_i = A_i T_g^{0.79} \ , \quad (i=1,2,3) \ . \tag{7b}$$

20

In Eq. (7b), T_g is the average temperature of the gap; A_i is 15.8×10^{-6}, 0.72×10^{-6} and 1.15×10^{-6} for He, and for fission gases Xe and Kr respectively, χ_i is the mole fraction of a particular gas in the mixture. In Eq. (6), the gap thickness, G, becomes zero when this equation is used in the closed gap equation. For the closed gap case, the thermal conductance due to solid to solid contact is given as:

$$h_s = \frac{C\,P}{H\sqrt{\delta_{eff}}} \, , \tag{8}$$

where C is a constant (0.01), P is the interfacial pressure (MPa) and H is the hardness of the softest material, which is Nb-1%Zr cladding. The effective gap thickness for closed gap, δ_{eff}, is given as:

$$\delta_{eff} = \sqrt{\left(\frac{\delta_f^2 + \delta_c^2}{2}\right)} \, . \tag{9}$$

Finally, the radiation contribution is given as:

$$h_r = \sigma \varepsilon_e \left(T_f^2 + T_c^2 \right) (T_f + T_c), \tag{10}$$

where σ is the Stefan-Boltzman constant (5.67×10^{-8} W/m$^2 \cdot$K^4), the effective surface emissivity, ε_e is calculated by:

$$\varepsilon_e = \left[\frac{1}{\varepsilon_f} + \frac{r_f}{r_c}(\frac{1}{\varepsilon_c} - 1) \right]^{-1} \, . \tag{11}$$

The volumetric heat generation in the fuel pin is allowed to vary in a cosine distribution in the axial direction. According to El-Wakil,[19] the volumetric heat generation at the geometrical center of a heterogeneous core, q'''_{co} can be calculated by:

$$q_{co}''' = \frac{P_F/1.05}{\left(\frac{4n}{\pi R_c^2}\right) A_s H_e \left(\frac{R_e}{2.4048}\right) \sin\left(\frac{\pi H}{2H_e}\right) J_1\left(\frac{2.4048 R_c}{R_e}\right)} \qquad (12)$$

where P_F, is the total fission power (or decay power) generated in the fuel region, n is the number of the fuel pins in the reactor, A_s is the cross section area of the fuel pellet in the pins, and H_e and R_e represent the extrapolated height and radius of the core. Since the normal neutron flux distribution is assumed in Eq. (12), the hottest fuel pin in the core is located at the center of the cylindrical core at r=0. The axial distribution of the volumetric heat generation for the fuel pin in the hottest channel at the center of the reactor core can be given as:

$$q'''(z) = q_{co}''' \cos\left(\frac{\pi z}{H_e}\right) \qquad (13)$$

The mass flow rate and coolant temperature in the reactor core are determined from the coupling of the fuel pin thermal model with the thermal-hydraulic model of the DHRL.

4.1.2 Method of Solution

The transient heat conduction equation (Eq. (1)), together with the boundary conditions (Eqs. (2a) and (2b)) and all the input parameters (Eqs. (3)-(13)), is solved in each axial segment of the fuel pin using a finite element method combined with an implicit time integrator.[9]

In each segment of a fuel pin, the transient one-dimensional heat conduction equation can be written as:

$$\rho_f C_f \frac{\partial T}{\partial t} - \frac{1}{r}\frac{\partial}{\partial r}\left(k_f r \frac{\partial T}{\partial r}\right) - q''' = 0 \qquad (14a)$$

Defining:

$$[T(r,t)] = \rho_f C_f \frac{\partial T}{\partial t} - \frac{1}{r}\frac{\partial}{\partial r}\left(k_f r \frac{\partial T}{\partial r}\right) - q''' \qquad (14b)$$

22

and using Gerlerkin Approximation,[21] Eq. (14a) can be written as:

$$\int_0^R N_i L[\ T^*(r,t)\ ]\ dr = 0$$

, (15)

where $T^*(r,t)$ is the approximation of $T(r,t)$ is the solution domain of $[0,R]$ which is defined as:

$$T^*(r,t) = \sum_{j=1}^M N_j(r)\ T_j(t)$$

. (16)

In Eq. (16), N_j is the basis function.[21] Substituting Eqs. (14a), (14b) and (16) into Eq. (15) and rearranging the result, yields:

$$\sum_{j=1}^M \left[\left(\int_0^R \rho_f C_f N_j(r) N_i(r) dr \right) \frac{dT_j}{dt} - \left(\int_0^R \frac{1}{r} N_i(r) \frac{\partial}{\partial r}(k_f r \frac{\partial N_j(r)}{\partial r}) dr \right) T_j(t) \right]$$

$$= \int_0^R N_i(r) q''' \ dr$$

, where $i,j = 1,2,...,M$. (17)

Equation (17) is equivalent to Eq. (14) under the Gerlerkin Approximation.[21] By choosing the basis function $N_i(r)$, we can solve Eq. (17) for $T_j(t)$, and then the approximate solution of $T(r,t)$ in $[0,R]$ domain, $T^*(r,t)$, can be calculated by Eq. (16). In Eq. (17), M is the number of elements used in the $[0,R]$ domain. Finally, the matrix form of Eq. (17) can be written as:

$$[C]\ \{\dot{T}\} = [K]\ \{T\} + \{Q\},$$ (18)

23

where

$$[C] = \begin{bmatrix} C_{1,1} & C_{1,2} & \cdots & C_{1,M} \\ C_{2,1} & C_{2,2} & & C_{2,M} \\ \vdots & \vdots & \ddots & \vdots \\ C_{M,1} & C_{M,2} & \cdots & C_{M,M} \end{bmatrix},$$

$$[K] = \begin{bmatrix} K_{1,1} & K_{1,2} & \cdots & K_{1,M} \\ K_{2,1} & K_{2,2} & & K_{2,M} \\ \vdots & \vdots & \ddots & \vdots \\ K_{M,1} & K_{M,2} & \cdots & K_{M,M} \end{bmatrix},$$

$$\{Q\} = \begin{Bmatrix} Q_1 \\ Q_2 \\ \vdots \\ \vdots \\ Q_{M-1} \\ Q_M \end{Bmatrix} \qquad \{T\} = \begin{Bmatrix} T_1 \\ T_2 \\ \vdots \\ \vdots \\ T_{M-1} \\ T_M \end{Bmatrix} \qquad \{\dot{T}\} = \begin{Bmatrix} \dfrac{dT_1}{dt} \\ \dfrac{dT_2}{dt} \\ \vdots \\ \dfrac{dT_{M-1}}{dt} \\ \dfrac{dT_M}{dt} \end{Bmatrix},$$

and the coefficients in these matrices are defined as follows:

$$C_{ij} = \int_0^R \rho_f C_f N_j(r) N_i(r) dr \quad ,$$

$$K_{ij} = \int_0^R \frac{1}{r} N_i(r) \frac{\partial}{\partial r} (k_f r \frac{\partial N_j(r)}{\partial r}) dr \quad ,$$

$$Q_{ij} = \int_0^R N_i(r) q''' \, dr \quad .$$

In Eq. (18), [C] is the capacitance matrix, [K] is the conductivity matrix, and {Q} is the heat source vector. The time integrator of the transient term on the right-hand side of Eq. (18) can be expressed as:

$$\{T\}^{n+1} = \{T\}^n + s[\alpha \{\dot{T}\}^{n+1} + (1-\alpha)\{\dot{T}\}^n] \quad , \tag{19}$$

where α is a constant determining the integration method and s is the time step size. As we can see in Eq. (19), α (which varies from zero-unity) represents the weight used for $\{T\}^{n+1}$ and $\{T\}^n$ to calculate $\{T\}^{n+1}$. The integration method is called 'fully explicit' for $\alpha = 0$ and 'fully implicit' for $\alpha = 1.0$.

Using Eq. (18) in both nth and (n+1)th time steps, the following final form of the matrix equation is obtained as:

$$([C] - s\alpha [K]) \{T\}^{n+1} = ([C] + s(1-\alpha)[K]) \{T\}^n + s\{Q\}^{n+1} \quad , \tag{20}$$

Solving this equation with the appropriate matrix decomposing algorithm gives the time dependent, two-dimensional temperature distributions inside the fuel pin for the given core coolant temperatures, coolant mass flow rate, and fission (or decay) power.

4.1.3 Model Verification

To verify the 2-D fuel pin, the calculated linear power distribution at steady-state is compared with the analytical value using in the equation:

$$q_l = 4\pi \int_{T_s}^{T_m} k_f(T) \, dT \tag{21}$$

where T_m and T_s are the calculated temperatures at the fuel centerline and the cladding surface respectively. For a cosine power profile $P(z) = P_0 \cos(\pi z / H_e)$, we calculated the linear power of the fuel pin using $q_l = P(z)/H_e$. These values are compared with the results calculated from Eq.(21) for a different mesh number. T_m and T_s are calculated using the 2-D fuel pin model at the same cosine power profile for UN fuel material. This comparison is presented in Figs. (11) and (12) for (10x10 = 100) meshes and (40x40 = 1600) meshes respectively. As these two figures show, for the 100 meshes case, the maximum difference between the numerical and analytical solution was 2.7% and for 1600 meshes was 0.044%. Increasing the mesh number increases the accuracy of the numerical results. However, 100 meshes still gives a reasonable accuracy and need much less CPU time for calculation compared with 1600 meshes. Therefore, in the subsequent analyses, a total of 10x10 meshes were used in the radial and axial direction of the fuel pin, respectively, to calculate its corresponding transient temperature profile.

4.2 Thermal-Hydraulics Model of the DHRL

The natural circulation thermal-hydraulic model of the DHRL (Figs. (7) and (8)) couples the reactor core, rise pipe (adiabatic section), decay heat exchanger (DHE), and down pipe and reactor downcomer (adiabatic sections). The energy and momentum balance equations are formulated and solved for the coolant bulk temperature within each region. These temperatures are used to update the coolant properties in the DHRL then, the overall momentum balance equation is solved for the coolant mass flow rate. This process continued, marching in time to calculate the coolant temperature and mass flow rate as a function of time after reactor shutdown.
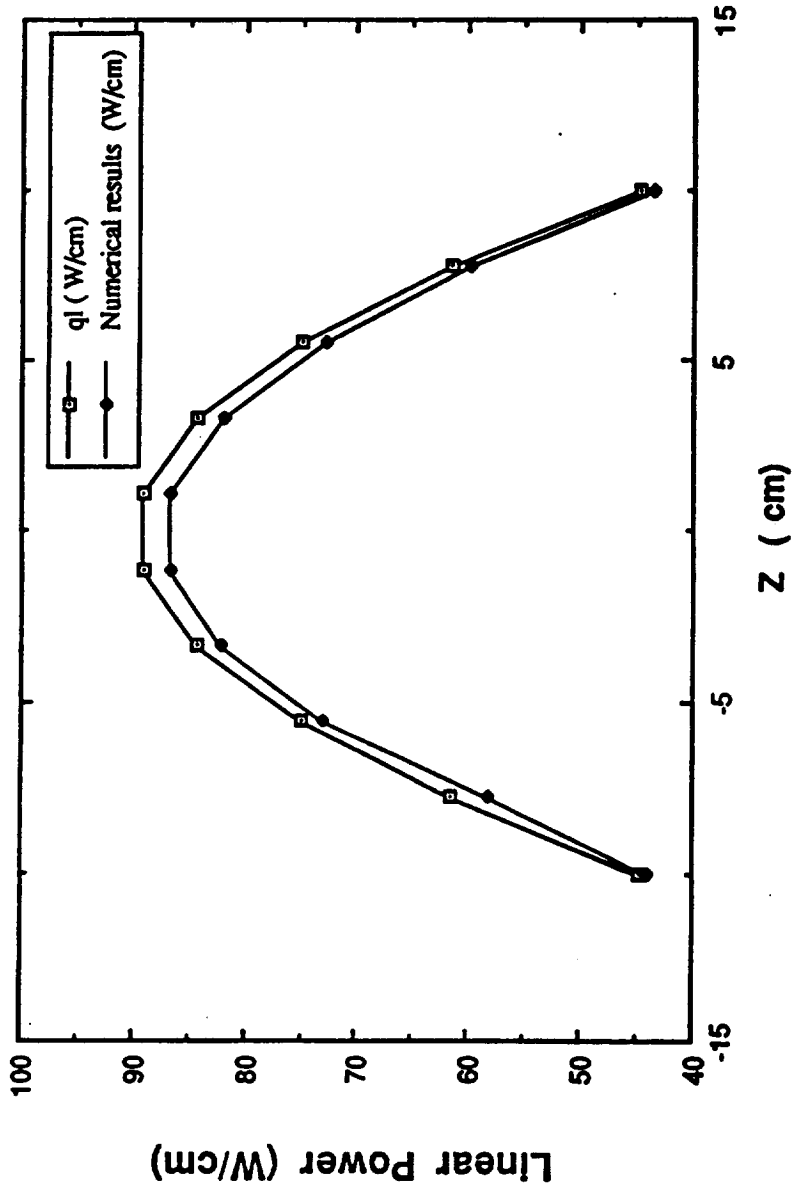
26

Fig. 11   Comparison of Linear Power Calculated by Thermal Power and
2-D Fuel Pin Model with 10x10 Meshes.

27
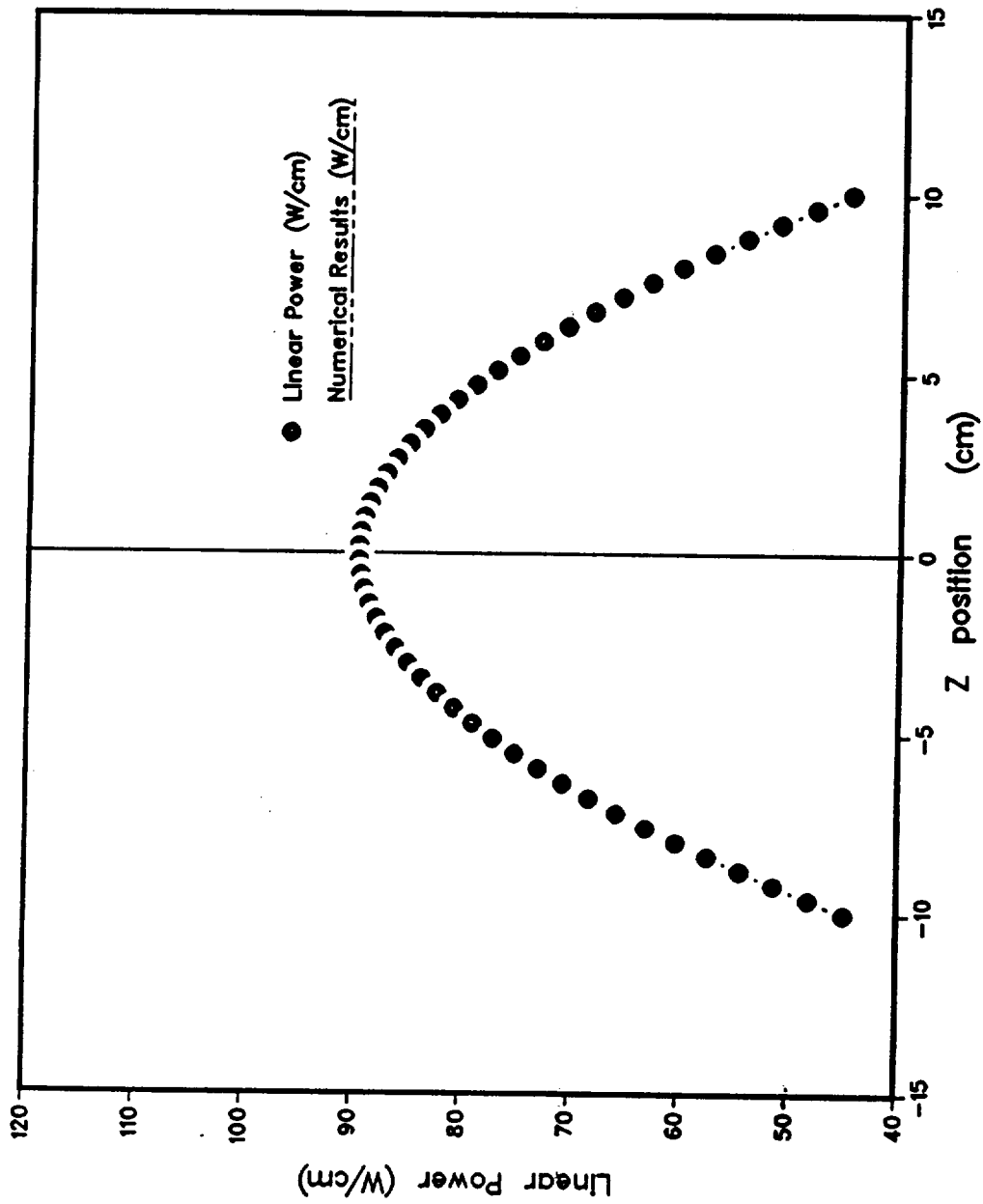
Fig. 12   Comparison of Linear Power Calculated by Thermal Power and 2-D
Fuel Pin Model with 40x40 Meshes.

28

4.2.1 Thermal Model

From the energy balance in a control volume of the DHRL, the general spatial distribution of the coolant bulk temperature in the DHRL can be determined by:

$$\rho_c C_c \left(\frac{\partial T_b(z,t)}{\partial t}\right) = \frac{\dot{m}}{A_s} \left(\frac{\partial T_b(z,t)}{\partial z}\right) - \left(\frac{U D_e}{4}\right) [T_b(z,t) - T_w(z,t)] + \frac{\partial}{\partial z}\left[k(z,t)\left(\frac{\partial T_b(z,t)}{\partial z}\right)\right] \qquad (22)$$

On the right hand side of Eq. (22), the first term and the third term correspond to axial convection and conduction heat transfer, respectively, and the second term is the radial heat transfer through the wall. In the reactor core, DHE and the adiabatic sections (rise/down pipes, reactor downcomer), the overall heat transfer coefficient, U, is calculated by different equations. In the core coolant flow channel, U is equal to h_l, which is calculated by Eq. (3), and in the DHE duct, U is determined as:

$$U = \left\{ A_i [(h_l A_i)^{-1} + (\delta_w/A_m k_w) + (h_r A_r)^{-1}] \right\}^{-1}, \qquad (23)$$

Where, the convective heat transfer coefficient, h_l is determined from the relations:[11]

$$Nu = 4.367, \qquad \text{for } R_e \leq 2,100, \qquad (24a)$$

and,

$$Nu = (2/3)Nu_s + 0.015 \, P_e^{0.8}, \quad \text{for } R_e \geq 3,000. \qquad (24b)$$

For $2,100 \leq Re \leq 3,000$, Nu is determined from a linear interpretation of Eqs. (24a) and (24b). The slug Nusselt number in Eq. (24b), Nu_s decreases with the aspect ratio of the DHE flow duct (a/b) increase (see Fig. (13)).[11] For the base case aspect ratio of 0.26 (see Table 1.), $Nu_s = 6.5$.[11]

29

The radiative heat transfer coefficient between the outer surface of the DHE wall and the inside surface of the guard vessel is given as:

$$h_r = \varepsilon \ \sigma \ F \ (T_w^2 + T_{hp}^2) \ (T_w + T_{hp}) \ . \tag{25}$$

The temperature of the guard vessel wall is assumed to be equal to that of the evaporator of the vessel's heat pipes, T_{hp}. The reactor decay heat is removed by thermal radiation heat exchange between the DHE and the guard vessel wall, which depends mainly on the temperature difference between these two components.

Because the rise/down pipes and the reactor downcomer (adiabatic sections) are thermally insulated, there is no heat loss in the radial direction from these components and, therefore, U is equal to zero. The only heat exchange in these components is through the convection and conduction in the axial direction.

To calculate the spatial distribution of the local coolant bulk temperature in the DHRL, each component in the loop is discretized into small spatial segments. Different components are discretized into different size segments. Non-uniform meshes are used for each component to keep the mesh size approximately the same at the junctions between components. In each segment, Eq. (22) is solved using a modified upwind finite difference method, which includes the contributions of both convection and conduction.[12] More detail will be discussed in the following sub-section.

4.2.2 Numerical Method for Solving the Energy Balance Equation of the DHRL

The DHRL is descritized into non-equal mesh size to accommodate the sudden change at the junctions between components. As shown in Fig. (14), the energy balance for the ith segment (control volume) can be expressed as:

$$M_i C_p^i \frac{dT_b^i}{dt} = (J_i A_s^i - J_{i+1} A_s^{i+1}) + A_i U_i (T_a^i - T_b^i) \ . \tag{26}$$

30

The left hand side of Eq. (26) is the specific heat change of the control volumn. In the right hand side, the first and the second terms are the net heat flux to the control volumn through axial convection and conduction and radial conduction respectively. Using the 'Power Law' scheme recommended by Patanka,[12] including the effects of convection and conduction, the heat flux density in the left and right boundaries of the ith segment, J_i and J_{i+1}, can be written as:

$$J_i = \frac{\dot{m}C_i}{A_s^i} T_b^{i-1} + D_{er}^i F(P_e^i)\,(T_b^{i-1} - T_b^i) \qquad , \qquad (27a)$$

$$J_{i+1} = \frac{\dot{m}C_{i+1}}{A_s^{i+1}} T_b^i + D_{er}^{i+1} F(P_e^{i+1})\,(T_b^i - T_b^{i+1}) \qquad , \qquad (27b)$$

where

$$P_e^i = \frac{\dot{m}C_i}{A_s^i D_{er}^i} \,. \qquad (27c)$$

Equation (27) is applied throughout the DHRL, except at the entrance of the core, z=0, where $J_i = J_{i+1}$.
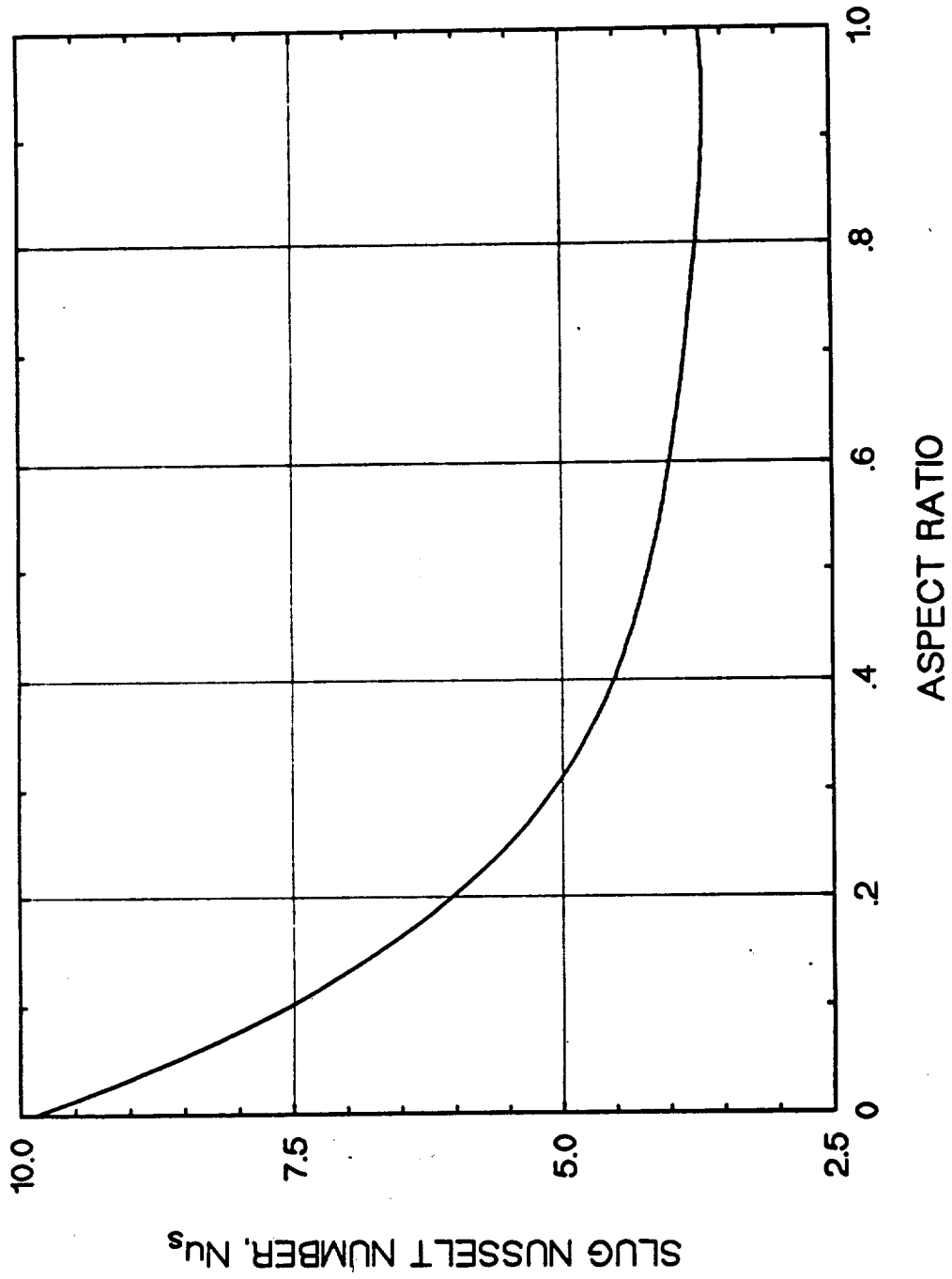
Fig. 13   The Correlation Between Slug Nusselt Number and Aspect Ratio.

32

In these equations, the coefficients D_{er}^i and D_{er}^{i+1} are the effect thermal conductances in the left and right boundaries of the control volumn respectively. $F(x)$ is a function considering dominate mode between convective and conductive heat transfer;[12] they are given as:

$$D_{er}^i = \frac{2}{\dfrac{\Delta h^{i-1}}{k_b^{i-1}} + \dfrac{\Delta h^i}{k_b^i}} ,$$

(27c)

$$D_{er}^{i+1} = \frac{2}{\dfrac{\Delta h^i}{k_b^i} + \dfrac{\Delta h^{i+1}}{k_b^{i+1}}} ,$$

(27d)

$$F(x) = Max\ (0,(1 - 0.1\,|x|\,)^5) + Max(0, -x).$$

(27e)

The function Max (a,b) is equal to the maximum value of a and b. Substituting Eqs. (27a) and (27b) into (26) and rearrange the results yields:

$$\frac{dT_b^i}{dt} = K_{i,i-1}T_b^{i-1} + K_{i,i}T_b^i + K_{i,i+1}T_b^{i+1} + Q_i .$$

(28)

Where N is the total number of control volumns in the DHRL.

$$K_{i,i-1} = \frac{\dot{m}C_i + D_{er}^i A_s^i F\ (P_e^i)}{M_i C_p^i} ,$$

(28a)

$$K_{i,i} = -\frac{D_{er}^i A_s^i F\ (P_e^i) + \dot{m}C_{i+1} + D_{er}^{i+1} A_s^{i+1} F\ (P_e^{i+1}) + h_i A_i}{M_i C_p^i} ,$$

(28b)

$$K_{i,i+1} = \frac{D_{er}^{i+1} A_s^{i+1} F\ (P_e^{i+1})}{M_i C_p^i} ,$$

(28c)

33

$$Q_i = \frac{h_i A_i}{M_i C_p^i} T_a^i \quad .$$

(28d)

Equation (22) was discretized into a set of algebra equations using a finite difference method. To solve these equations, Eq. (28) was in a matrix format as follows:

$$\{\dot{T}_b\} = [K] \{T_b\} + \{Q\} ,$$

(29)

where:

$$\{\dot{T}_b\} = \begin{Bmatrix} \dfrac{dT_b^1}{dt} \\ \dfrac{dT_b^2}{dt} \\ \vdots \\ \dfrac{dT_b^N}{dt} \end{Bmatrix} , \qquad \{T_b\} = \begin{Bmatrix} T_b^1 \\ T_b^2 \\ \vdots \\ T_b^{N-1} \\ T_b^N \end{Bmatrix} , \qquad \{Q\} = \begin{Bmatrix} Q_1 \\ Q_2 \\ \vdots \\ Q_{N-1} \\ Q_N \end{Bmatrix} , \text{ and}$$

$$[K] = \begin{bmatrix} K_{1,1} & K_{1,2} & \cdots & K_{1,N} \\ K_{2,1} & K_{2,2} & & K_{2,N} \\ \vdots & \vdots & \ddots & \vdots \\ K_{N,1} & K_{N,2} & \cdots & K_{N,N} \end{bmatrix} .$$

The operator, [K] is a tri-diagonal matrix, except that $K_{1,N}$ and $K_{N,1}$ are not zero.

To calculate the transient coolant bulk temperature in the DHRL, T_b, Trapezoidal time integrator was applied:

34

$$\{T_b\}^{n+1} = \{T_b\}^n + s\left[\alpha \{\dot{T}_b\}^{n+1} + (1-\alpha)\{\dot{T}_b\}^n\right] . \tag{30}$$

In Eq. (30) $\{\dot{T}_b\}^n$ and $\{\dot{T}_b\}^{n+1}$ are obtained by using Eq. (29) in nth and (n+1)th time steps as:

$$\{\dot{T}_b\}^n = [K]^n \{T_b\}^n + \{Q\}^n, \tag{31}$$

$$\{\dot{T}_b\}^{n+1} = [K]^{n+1} \{T_b\}^{n+1} + \{Q\}^{n+1} , \tag{32}$$

combining Eqs. (30), (31) and (32), yields the following general form:

$$\left([I] - s\alpha [K]^{n+1}\right)\{T_b\}^{n+1} = \left([I] + s(1-\alpha)[K]^n\right)\{T_b\}^n$$
$$+ s\left[\alpha \{Q\}^{n+1} + (1-\alpha)\{Q\}^n\right] . \tag{33}$$

Because thermal conductance matrix [K] is a function of coolant bulk temperature, Eq. (33) is a nonlinear equation. It was solved using a iterating method with fully implicit scheme ($\alpha = 1.0$).

4.2.3 Hydraulics Model

The coolant mass flow rate in the DHRL, by natural circulation after shutdown of the nuclear reactor, is determined from the overall momentum balance equation in the DHRL as follows [see Appendix B]:

$$\int_L (\frac{d\dot{m}}{dt})dz = \int_L \rho g_m A(z)dz - \int_L A(z)dP_{loss} . \tag{34}$$

The integrations in Eq. (34) are carried out over the entire DHRL. The pressure loss term on the right hand side of Eq. (34) includes losses due to friction, pipe expansion and contraction, and acceleration losses of the coolant in the DHRL.
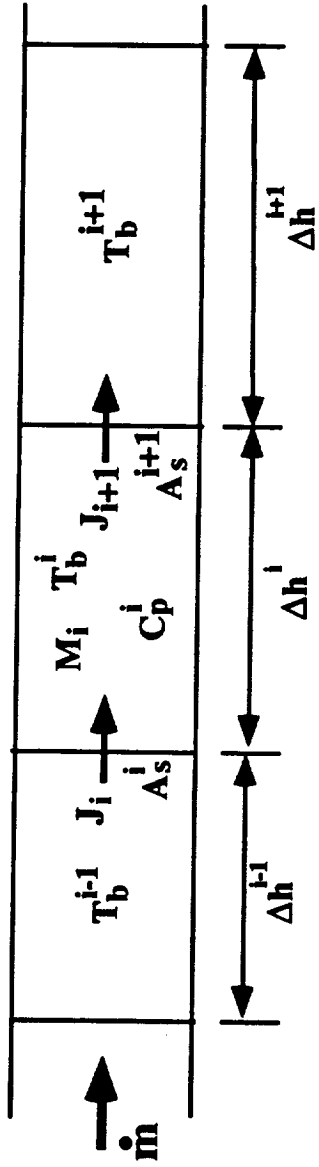
35

Fig. 14   Meshes in Decay Heat Removal Loop.
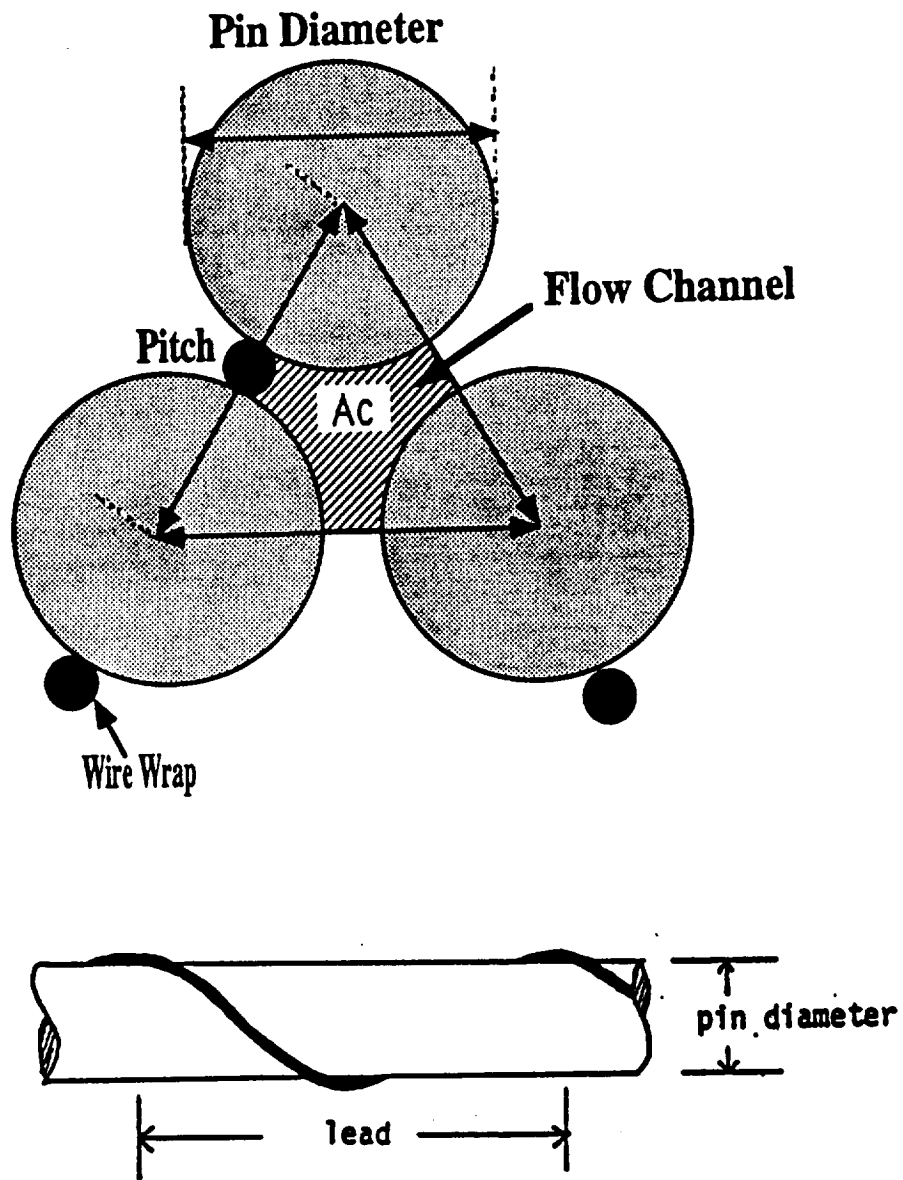
Fig. 15   Reactor Core Flow Channel and Wire Wrapped Fuel Pin.

37

In the reactor core region, all the flow channels are assumed to be identical as shown in Fig. (15). Therefore, the difference in flow rate between the center channels and the edge channels is negligible. The pressure losses in the core is calculated using the CRT (Chui-Rohsenow-Todreas) model for the triangular pitched channel with wire wrapped fuel rods:[13]

$$\Delta P_{loss}^{core} = f_s \left(\frac{H_c \dot{m}^2}{2 D_e A_c^2 \bar{\rho}_c} \right) \left[1 + C \frac{A_c D_e P^2}{\bar{A} H_c (\pi P^2 + H_c^2)} \right],$$

(35)

where the friction factor, f_s, is based on the pressure drop in the flow channel without a wire wrap, and

$$D_e = \frac{2\sqrt{3} P^2 - \pi (D_f^2 - s^2)}{\pi (D_f + s)},$$

(36)

$$A_c = \frac{\pi s}{6} (D_f + s), \quad \text{and} \quad \bar{A} = \frac{\sqrt{3}}{4} P^2 - \frac{\pi D_f^2}{4}.$$

(37)

In the pipes, reactor downcomer, and the DHE duct, the friction losses are calculated using Blasius relation for smooth walls:

$$\Delta P_{loss}^{pipe} = \sum_i \frac{\Delta L_i}{D_e} f_s \frac{\dot{m}^2}{2 \rho_c^2 A_c^2},$$

(38)

where the friction coefficient is given as:

$$f_s = (64/Re), \quad \text{for } Re \le 2{,}100,$$

(39a)

$$f_s = -0.001476 + 1.522 \times 10^{-5} Re, \quad \text{for } 2{,}100 \le Re \le 3{,}000,$$

(39b)

$$f_s = 0.0058 + 0.05 / Re^{0.32}, \quad \text{for } 3{,}000 < Re < 3 \times 10^6.$$

(39c)

The curve of f_s vs Re is shown in Fig. (16). In this figure the boundaries of each flow regions are illustrated.

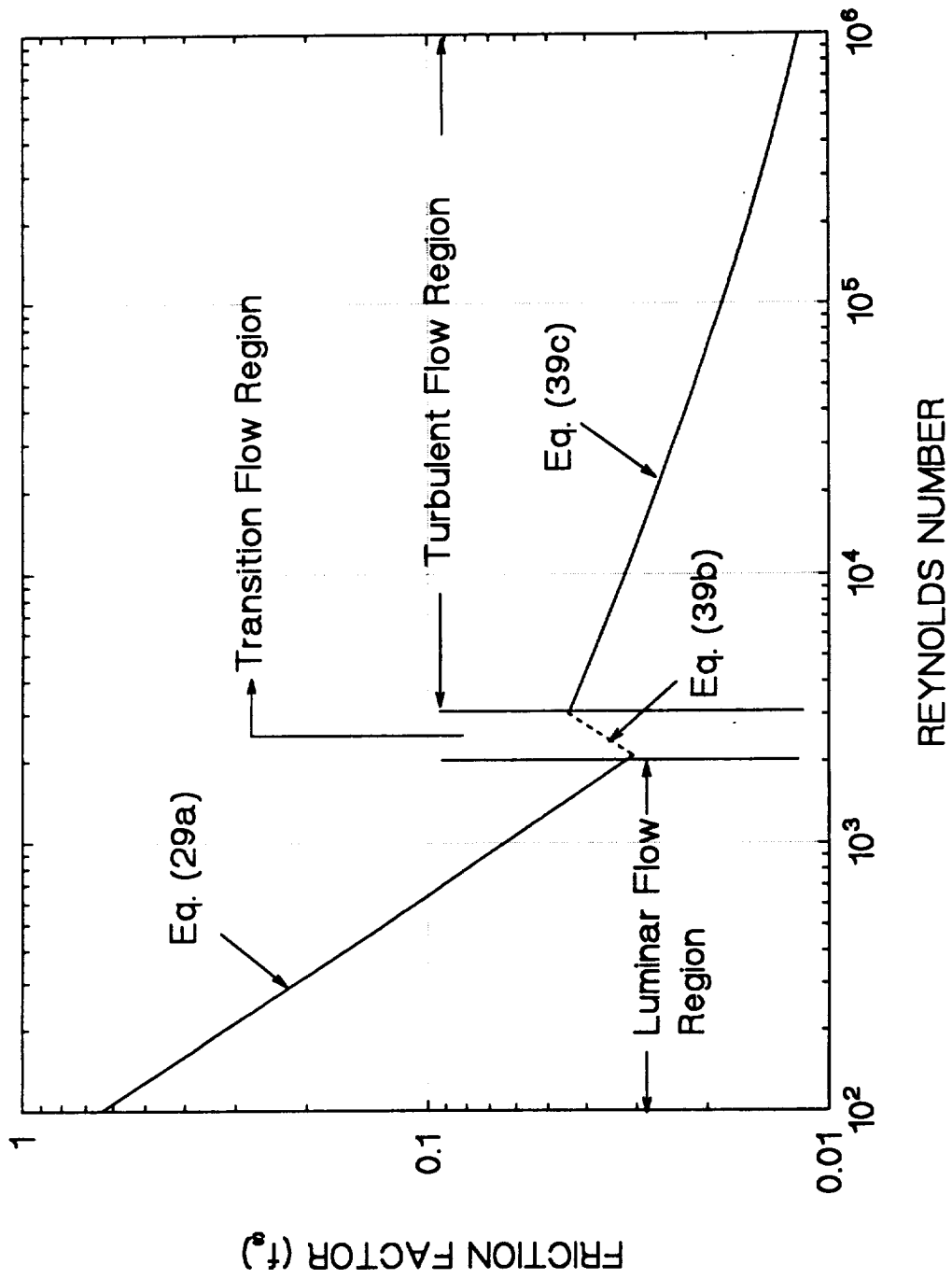Fig. 16   Friction Factor as a Function of Reynolds Number.

Equations (22) and (34) are solved iteratively to determine the coolant mass flow rate and the spatial distribution of the local coolant bulk temperature in the DHRL as functions of time after reactor shutdown. The numerical algorithm is explained in the block diagram of Fig. (17).
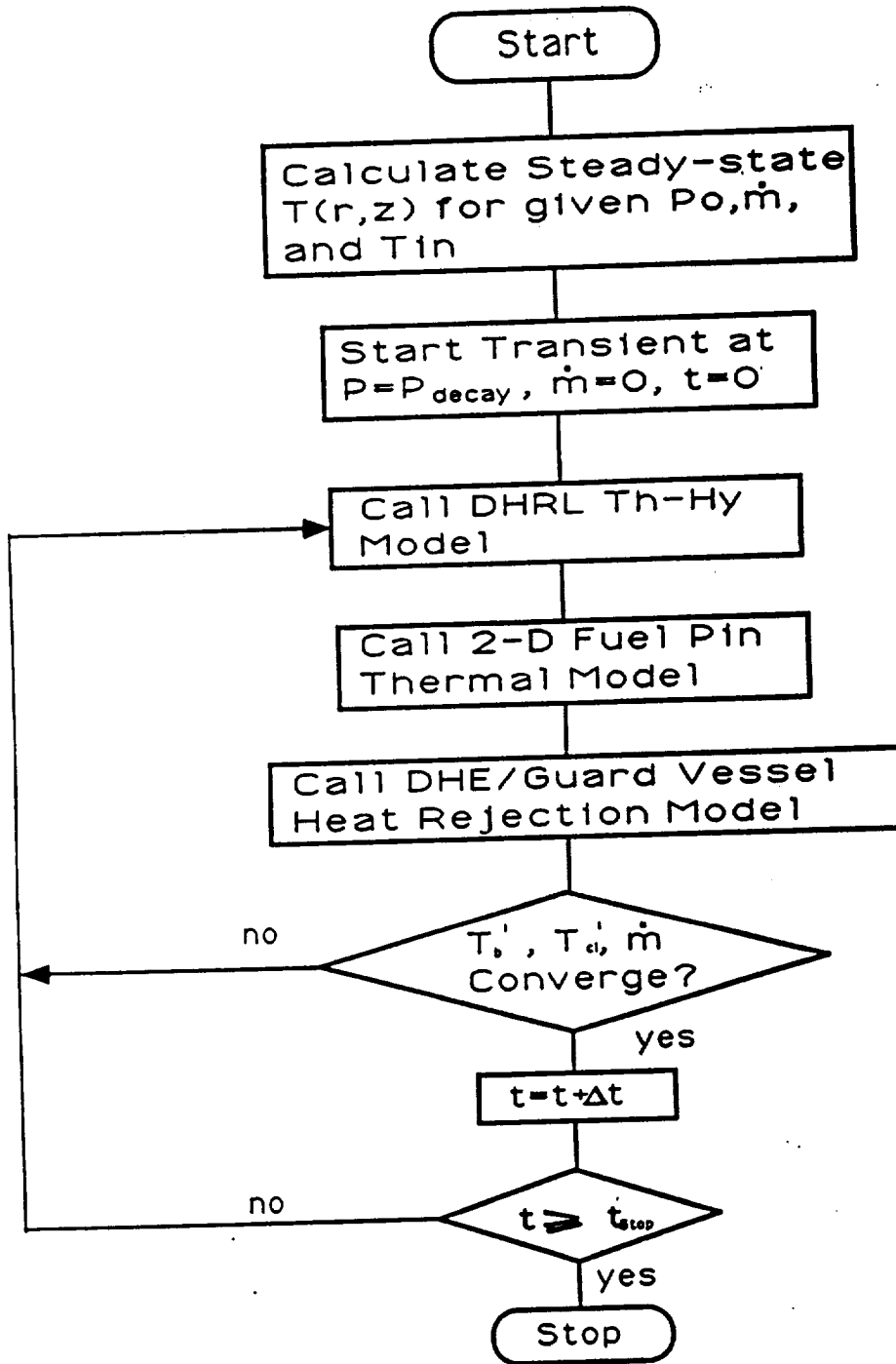

Fig. 17   A Block Diagram for the Algorithm of the DHRL Model.

40

4.3 DHE/Guard Vessel Heat Pipes Heat Rejection Model

As indicated earlier, the DHE is radiatively coupled to the inside surface of the guard vessel. The heat removal from the DHE, and hence the coolability of the SP-100 reactor after shutdown, depends on both the energy transport capability of the guard vessel heat pipes to the decay heat radiators and the heat rejection capacity of the latter. At any time step in the transient numerical solution, the temperature of the guard vessel heat pipes, T_{hp}, is determined from a quasi steady-state heat balance between the DHE and the guard vessel as:

$$\int_{DHE} \frac{4A_s h}{D_e} (T_b(z,t) - T_{hp}) \, dz = Q_{rej}, \tag{40a}$$

where,

$$Q_{rej} = h_r A_r (T_{hp} - T_a), \text{ or } P_{sonic}(T_{hp}) . \tag{40b}$$

However, the temperature of the guard vessel heat pipes is determined by the dominant mode of heat transport, radiator heat rejection, $Q_{rej} = h_r A_r (T_{hp} - T_a)$, or the sonic limit of guard vessel heat pipes, $Q_{rej} = P_{sonic}$.[7,9]

At the sonic limit, the vapor flow at the exit of the evaporator region of the heat pipe is choked, where the flow velocity is equal to the sonic speed of the vapor at the evaporator temperature; T_{hp}. The maximum power throughput due to the sonic limit is given by:[23]

$$P_{sonic} = 0.474 \, A_{hp} h_{fg} \sqrt{\rho_v \, p_v} , \tag{40c}$$

where h_{fg}, ρ_v and p_v for the heat pipe working fluid are evaluated at T_{hp}.

Initially, following the reactor shutdown, the guard vessel heat pipes temperature is such that heat rejection by thermal radiation from the decay heat radiators to the ambient on the lunar surface is lower than the energy transport by the vessel heat pipes at the sonic limit. In this case, the decay heat removal

41

from the reactor core is restricted by the surface area of the decay heat radiators (see Fig. (18)). However, as the decay heat power decreases with time, both the guard vessel wall temperature and the sonic limit of the vessel heat pipes will decrease. Eventually, as the sonic limit of the heat pipe drops below that of the decay heat radiator, the heat removal from the DHRL will be restricted by the sonic limit of the heat pipes. That will slow down the heat removal from the SP-100 reactor core (see Fig. (18)).

Although the heat pipe sonic limit would slow down the decay heat removal from the reactor core, it could prolong the time for the lithium coolant to cool down to its freezing temperature.[14] Lithium freezing in the primary loop is not desirable because the formation of voids during freezing could induce hot-spots in the reactor core during a subsequent startup.[15-17] Therefore, guard vessel heat pipes sonic limit can be used to prevent the lithium freezing with a sacrifice on the decay heat removal capability of the DHRL system. The designers must make some compromise in these two aspects.

For different heat pipe working fluids (water, potassium and sodium) and heat pipe diameter, the heat pipe code HTPIPE[20] is used to calculate the sonic limits for the guard vessel heat pipes at the evaporator temperature and the results are presented in Fig. (18). The heat rejected from the decay heat radiator with a different surface area is calculated as a function of the radiator temperature and the results are also present in Fig. (18). We assumed the temperatures of the guard vessel heat pipes and of the decay heat rejection radiator are equal. As delineated in this figure, for a decay heat radiator surface area of 25 m^2, the potassium heat pipes of 2.54 cm diameter in the guard vessel heat pipes reach their sonic limit at an evaporator temperature of 777 K. This transition temperature, from a radiator limited heat removal to a heat pipe limited heat removal, increases as the radiator area increases. Fig. (18) also demonstrates that water heat pipes are unsuitable for cooling the guard vessel walls because the wall temperature would initially exceed the critical temperature of water (~ 550 K) for a medium decay heat radiator (such as 25 cm^2, see the discussion in Section 5). Therefore, potassium heat pipes are a better choice for cooling the guard vessel wall. The effect of the transition from a radiator limited heat rejection to heat pipes limited heat rejection on the coolability of the DHRL is included in the decay heat removal model. In our analysis, potassium heat

42
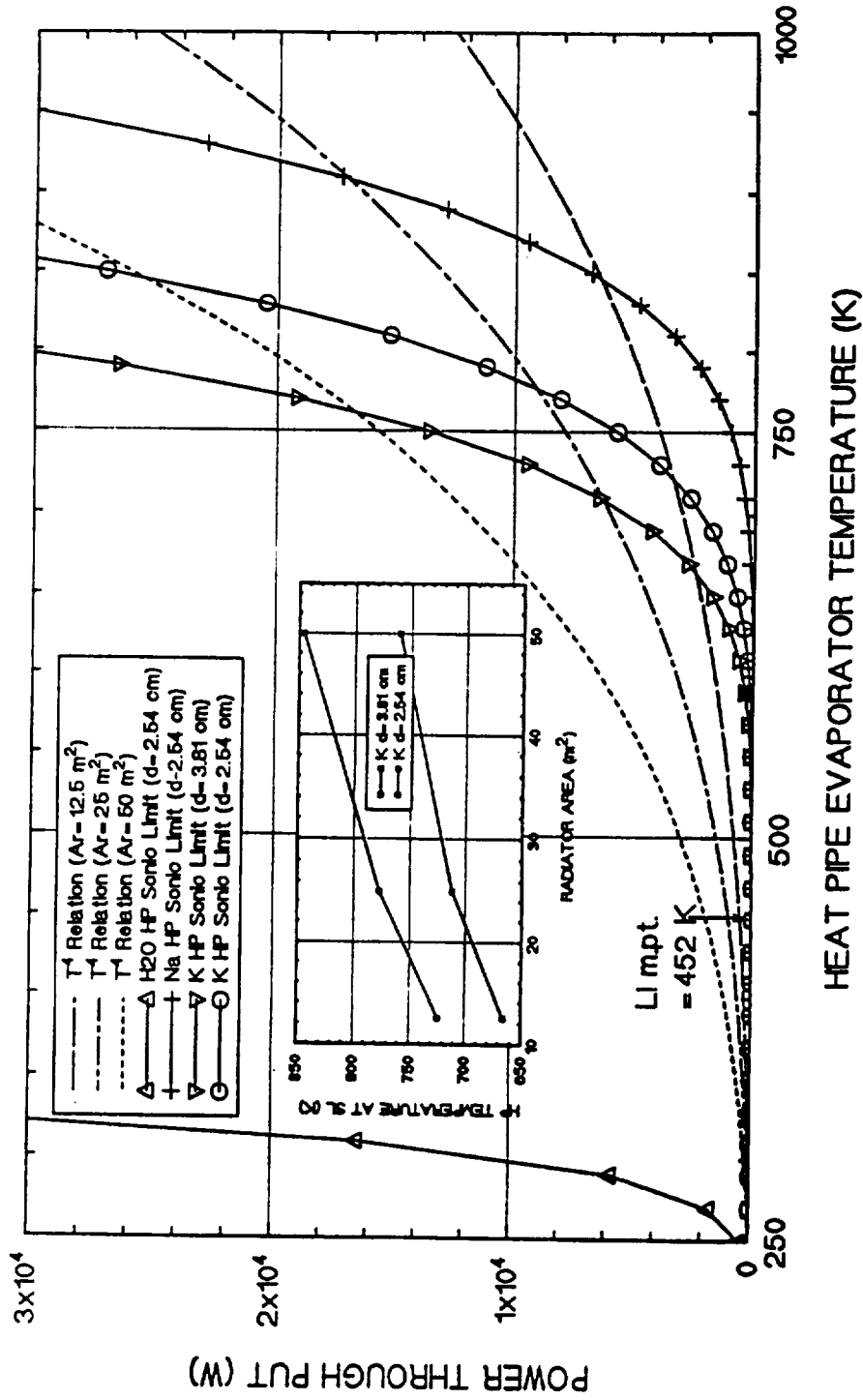
Fig. 18   Effects of Diameter and Working Fluid of the Guard Vessel Heat
Pipes on Decay Heat Rejection.

43

pipes are used to transport the heat from the guard vessel wall to the decay heat radiator on the lunar surface.

In this section, the transient overall momentum and energy balance equations of the DHRL described, together with the transient heat conduction equation in the fuel pin are solved interactively using a fully implicit time integrator. The coupled decay heat removal model calculates the spatial distribution of the local bulk temperature of Li coolant in the DHRL as well as the axial and radial temperature distributions in the fuel pin, as functions of time after reactor shutdown. In the following section, the results of the analyses investigating the coolability of the SP-100 reactor core after shutdown by natural circulation on the lunar surface are presented for the base case design and operation parameters listed in Table 1. The parametric analyses of the effects of the design parameters of the DHRL on the decay heat removal capability of the system are also performed and the results are included in the next section.

5. RESULTS AND DISCUSSION

This section includes three parts. The first part presents the results of some transient analyses of the passive decay heat removal capability of the DHRL of the SP-100, 550-kW$_e$ power system for a lunar outpost following a LOFA. In the second part, the results of the parametric analyses for some design parameters of the DHRL are presented and discussed. In the last part, the differences and similarities of the thermal behavior of the system after shutdown at two gravity constants (1g and 1/6 g) are discussed. These results would be useful in relating earth-based preflight test results to the actual system performance on the lunar surface.

5.1 Base Case Result

The base case design and operation parameters for the SP-100, 500-kWe power system for a lunar outpost, listed in Table 1., are based on the information provided by Rockwell International Corp.[22] The envelop dimensions of the reactor and the shield are shown in Fig. (19). The nominal thermal power of the SP-100 reactor is about 2.3 MW thermal, at which the coolant temperature at the exit of the reactor core is ~ 1355 K. The reactor core consists of approximately 1296 fuel pins in a triangular arrangement.

The initial condition for our calculation is based on the following hypothesis: At a time when the SP-100 reactor is operating at its nominal power level, the reactor scrams, and at the same time, the lithium coolant mass flow rate drops to zero (LOFA). Therefore, the vanturi allows natural circulation of lithium coolant through the DHE initiated by the density difference between the rise and down pipes. To be practical, the coolant mass flow rate may not drop to zero at the same time of reactor scram. These initial conditions should be considered as the worst case in a LOFA.
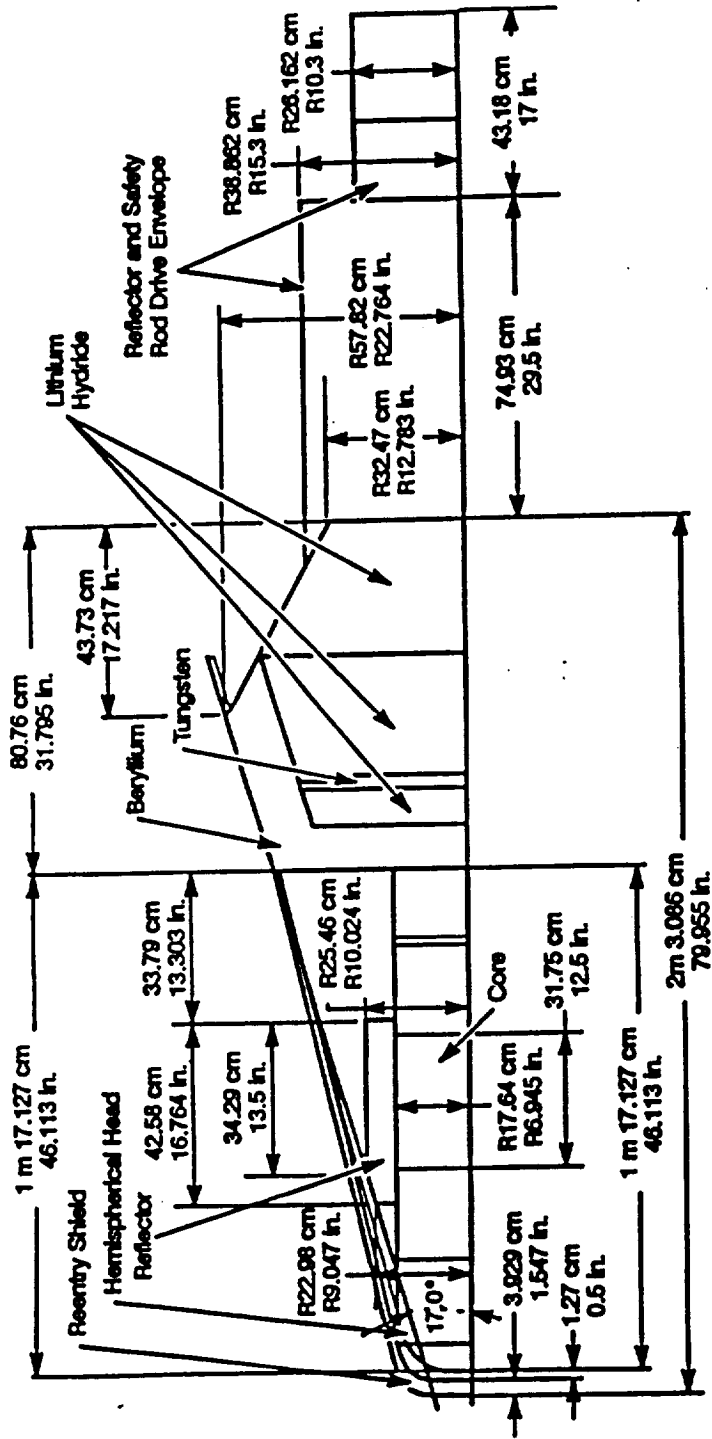
45

Fig. 19   Dimensions of the SP-100 Reference Flight System Reactor.

5.1.1 Spatial Coolant Temperature Distribution

Figure (20) presents the calculated spatial distributions of the local bulk temperatures of Li coolant in the DHRL at different times after reactor shutdown. The steep temperature gradients at the interfaces between the reactor core, both the adiabatic rise and down pipes, and between these pipes and the DHE, clearly demonstrate that the effect of axial heat conduction in the Li coolant flow is important for the heat transport in the DHRL by natural circulation. As indicated in Fig. (20), immediately after reactor shutdown, the maximum coolant temperature in the DHRL (~ 1355 K) occurs at the exit of the reactor core. This is also the case during full power operation, where forced convection is the dominant mode of heat transfer. However, since the coolant flow rate by natural circulation is much lower than that at full power operation (see Fig. (22) and Table 1.), the contribution of axial heat conduction in the liquid metal coolant, immediately after shutdown, becomes important. The axial heat conduction in Li coolant, together with convective heat transfer, causes the maximum coolant temperature in the DHRL to increase (up to 100 seconds after shutdown) and shift with time away from the exit of the SP-100 reactor core toward the DHE.

As shown in Fig. (20), it takes about 200 seconds for the hottest part of the Li coolant (with the maximum coolant temperature) to travel from the exit of the reactor core to the entrance of the DHE. In addition to being shifted toward the DHE, the temperature of the hottest part of Li in the DHRL decreases with time after shutdown from a peak value of 1530 K, happened at about 50 seconds after shutdown, to about 1250 K after 300 seconds.

The results in Fig. (20) also show that at times greater than 200 seconds after shutdown, the maximum coolant temperature in the DHRL occurs at the entrance of the DHE, while the lowest coolant temperature always occurs at the exit of the DHE. This is because the DHE acts as a heat sink in the DHRL after the reactor shutdown. The lowest coolant temperature also decreases from approximately 1275 K, immediately after shutdown, to about 900 K after 300 seconds. Despite the rapid decrease in decay power in the reactor core with time after shutdown, the average coolant temperature in the DHE decreases much slower. Such a slow decrease in the coolant temperature in the DHRL after
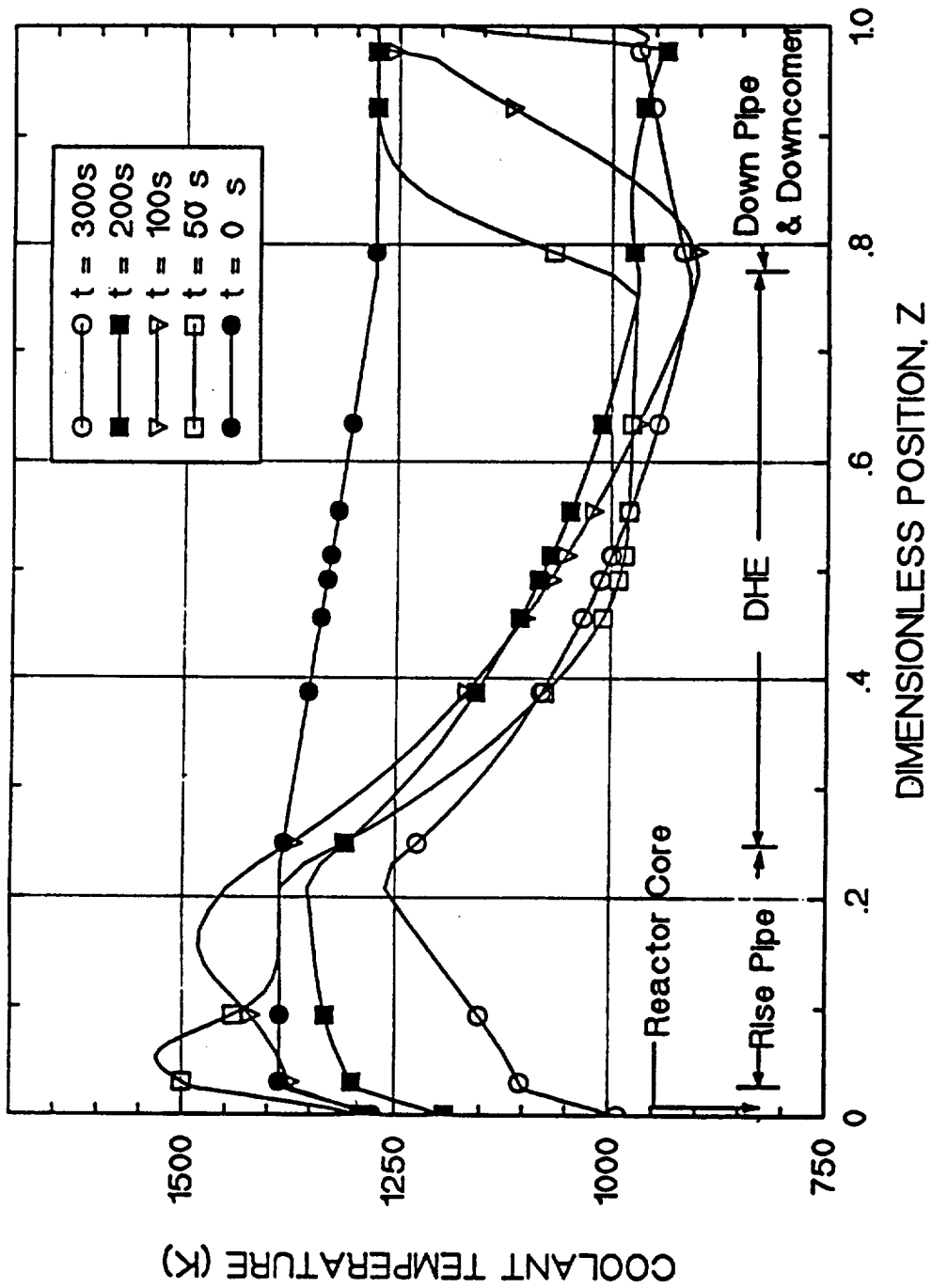
47

Fig. 20   Spatial Distribution of the Lithium Coolant in the DHRL After
Reactor Shutdown on the Lunar Surface.

48

reactor shutdown is because of the large heat capacity of the lithium coolant (> 4.5 kJ/kg K) and a very low coolant mass flow rate. Although the maximum coolant temperature in the DHRL does not drop below its value at full power operation (~1355 K, see Table 1.) before 50 seconds after shutdown, the coolant temperature in the reactor core insignificantly increases above its value during full power operation, instead it drops very rapidly after shutdown.

It is worth noting that during the first 100 seconds (even more) after the reactor shutdown, the coolant temperatures in the rise pipe is higher than its value during nominal full operation. Sometimes (like ~ 50 seconds after shutdown), its maximum value is as much as 175 K higher than its nominal value. This temperature increase might contribute to some undesired effects (such as boiling in the lithium coolant or creep in the pipe walls) in the system.

Figure (21) shows the axial variation in the centerline temperature of a fuel pin at the center of the reactor core after shutdown. As this figure indicates, after shutdown, the maximum fuel temperature always occurs at the exit of the reactor core and decreases to a relatively lower temperature (< 1200 K) after 300 seconds following reactor shutdown.

5.1.2 Transient Maximum Coolant and Fuel Pin Temperatures

Figure (22) compares the calculated maximum coolant temperatures in the DHRL with those of the fuel and cladding in the SP-100 reactor core after shutdown. Also delineated in Fig. (22) are the calculated time dependent temperatures of the guard vessel (or its heat pipes) and the coolant mass flow rate by natural circulation in the DHRL. As this figure shows, the maximum fuel temperature drops very rapidly from its nominal value of about 1950 K at full power operation (see Table 1.), to about 1500 K within the first 5 seconds after shutdown. At such time, the very low coolant flow rate by natural circulation results in the removal rate of the decay heat from the fuel pins being lower than its rate of generation, causing the maximum fuel temperature, at the centerline of the fuel pin to rise reaching a maximum of ~1600 K at 30 seconds after shutdown. Beyond this point, the decay heat generation rate drops below the rate of removal by natural circulation, causing the maximum fuel temperature to decrease with time, reaching as low as 1000 K at 1000 seconds after shutdown.
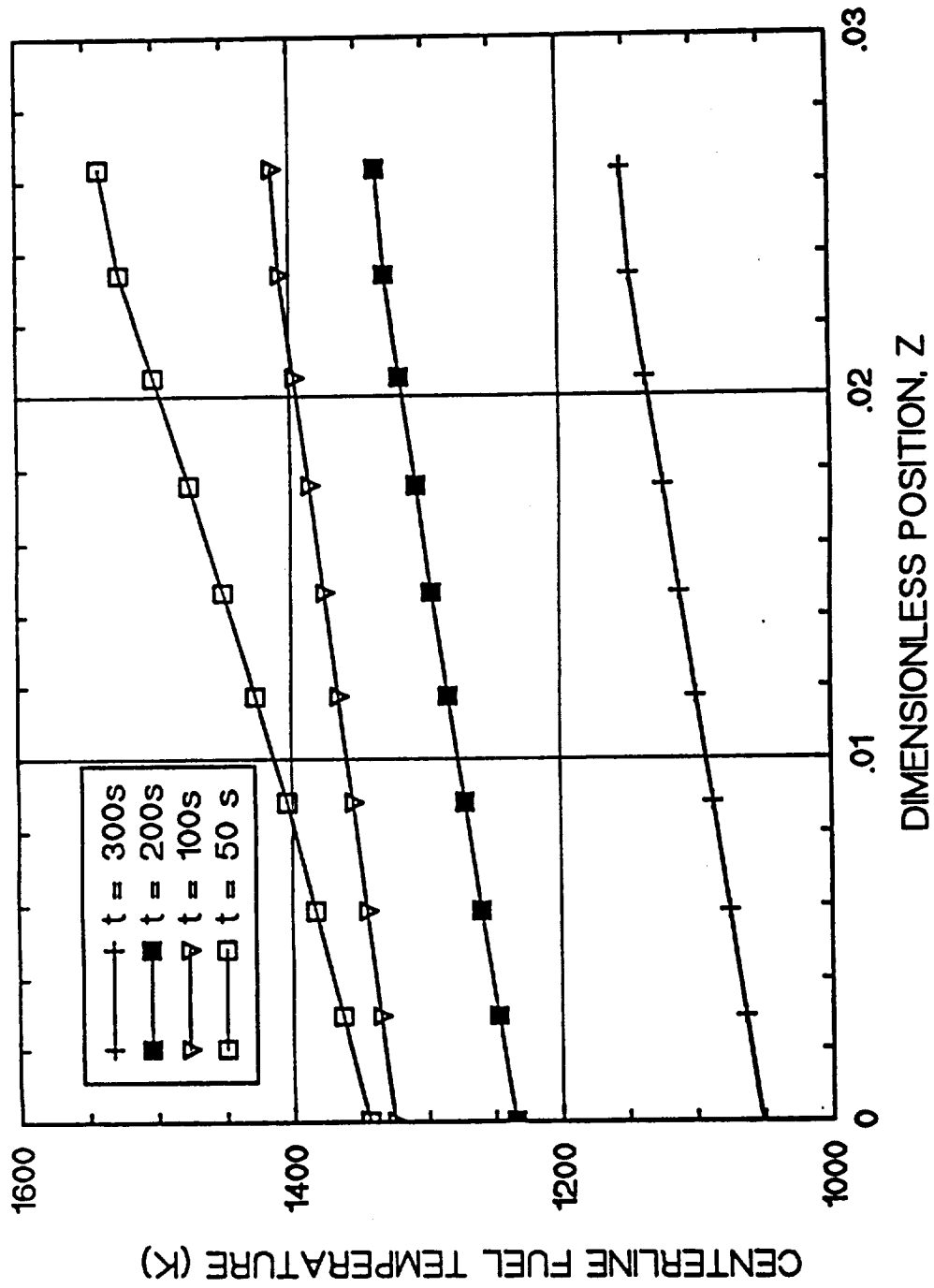
49

Fig. 21   Axial Distribution of the Fuel Pin Centerline Temperature as a Function of Time After Shutdown.
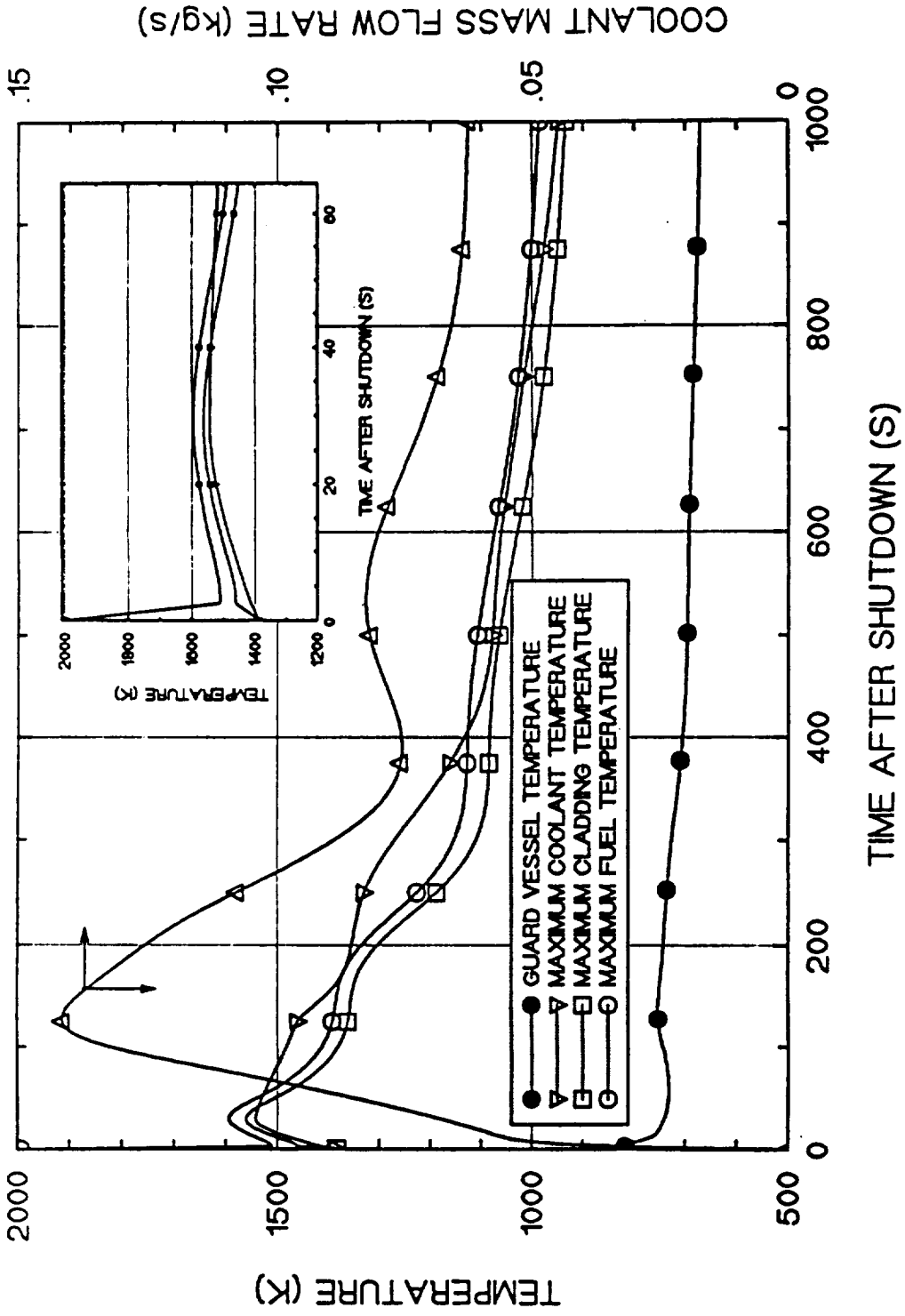
50

Fig. 22   Calculated Maximum Coolant, Fuel, and Cladding Temperatures and
Coolant Mass Flow Rate in the DHRL as Functions of Time after
Shutdown.

51

Results in Fig. (22) indicate that, while the maximum temperature of the coolant in the DHRL peaks shortly after shutdown (~ 30 seconds), the coolant mass flow rate by natural circulation takes up to 120 seconds to reach a maximum value of ~0.14 kg/s. This increase in the coolant mass flow rate occurs when the hot coolant from the reactor core travels through the adiabatic rise pipe(see Fig. (7)). The induced density difference between the hot liquid in the rise pipe and the cold liquid in the down pipe causes the coolant mass flow rate in the DHRL to increase with time. It reaches a maximum value of 0.14 kg/s as the hot coolant enters the DHE duct. When the hot coolant exits the rise pipe and travels through the DHE duct, its temperature decreases and hence the buoyant force for natural circulation, causes the coolant mass flow rate to decrease. Such a decrease in the coolant mass flow rate continues until the coolant from the DHE begins to travel through the down pipe toward the reactor core. This occurs at about 400 seconds after shutdown, at which time the coolant mass flow rate reaches a minimum value of ~ 0.075 kg/s. When the coolant from the DHE fills the down pipe, the density difference between the hot coolant in the rise and the cold coolant in the down pipe increases, causing the coolant mass flow rate to increase again; it reaches a second, but much lower, peak value of ~ 0.082 kg/s, at approximately 520 seconds after shutdown. This response of the coolant mass flow rate continues each time when the cold coolant from the DHE travels through the down pipe. However, the peak mass flow rate decreases progressively with time after shutdown, commensurate with the decrease in decay power. Such a variation in the coolant mass flow rate in the DHRL is responsible for the variations shown in the coolant, fuel, and cladding temperatures delineated in Fig. (22).

While the responses of the maximum cladding and coolant temperatures are similar to that of the maximum fuel temperature, the temperature of the guard vessel wall generally decreases very slowly after shutdown (see Fig.(22)). Such slow decrease in the guard vessel heat pipe temperature, particularly at times in excess of ~120 seconds after shutdown, is because the decay heat removal from the DHRL is constrained by the sonic limit of the guard vessel heat pipes. Conversely, during the first 120 seconds after shutdown the decay heat removal from the DHRL is constrained by the decay heat radiator (surface area and temperature) on the lunar surface, causing the guard vessel wall temperature to

52

decrease at a relatively higher rate. This thermal behavior will be discussed in the second part of this section.

The above-mentioned results suggest that natural circulation of lithium coolant in the DHRL of the SP-100, 550-kWe power system for a lunar outpost would maintain the SP-100 reactor core safely coolable after shutdown. However, the lithium coolant in the adiabatic rise pipe, directly downstream of the reactor core, could be overheated by as much as 175 K, above its nominal operation value, for approximately 200 seconds after shutdown. The effect of such temperature overheating on the structure strength of the rise pipe walls should be assessed before a final conclusion can be drawn regarding the coolability of the DHRL by natural circulation of lithium coolant. In the second part of this section, the effects of changing some design parameters of the DHRL on improving the coolability of the DHRL are being investigated.

5.2 Parametric Analyses of the Coolability of the DHRL

In this sub-section, the decay heat removal model is used to examine the effects of the following parameters on the decay heat removal capability of the system: (a) the height of the DHE duct; (b) the elevation of DHE; (c) the diameter of DHRL pipes; (d) the surface area of the decay heat rejection radiator on the lunar surface; and (e) the diameter of the guard vessel heat pipes. In the previous sub-section, it was shown that the maximum coolant temperature of the DHRL could be as much as 175 K above its nominal value with the decay heat removed by natural circulation after reactor shutdown. Other components' temperatures are found to be below their nominal values during full power operation. Therefore, the maximum coolant temperature after shutdown will be taken as the criterion for assessing the coolability of the system.

5.2.1 Effect of DHE Dimensions

Figure (23) presents the results on the effects of changing the height of the DHE duct, with the same aspect ratio (see Table 1.), and the surface area of the decay heat radiator on the coolability of the DHRL by natural circulation after shutdown. In the base case, the height of the DHE rectangular duct is 10 cm (see Table 1.), for which the maximum coolant temperature in the DHRL exceeds

1550 K after reactor shutdown. However, in order for this temperature to be brought closer to its value during nominal operation of the power system (1355 K), the height of the DHE is increased. In addition to increasing the surface area of DHE, such increase in the duct height reduces friction losses, resulting in a higher coolant flow rate and lower coolant temperature. Conversely, increasing the height of the DHE duct beyond 20 cm, increases friction pressure losses, hence reducing the mass flow rate. This increase in friction losses is because the coolant flow will be in the transitional regime, where $2100 < Re < 3000$ (see Eq. (39b)). Results shown in Fig.(23) also indicate that increasing the height of the DHE duct beyond 15 cm, the resulting decrease in the maximum coolant temperature is very small, hence that the change in the DHE duct height, when it is beyond 15 cm, will insignificantly affect the coolability of the DHRL. At such a duct height, the maximum coolant temperature in the DHRL after reactor shutdown is about 1480 K, which is still about 125 K higher than that at full poweroperation.
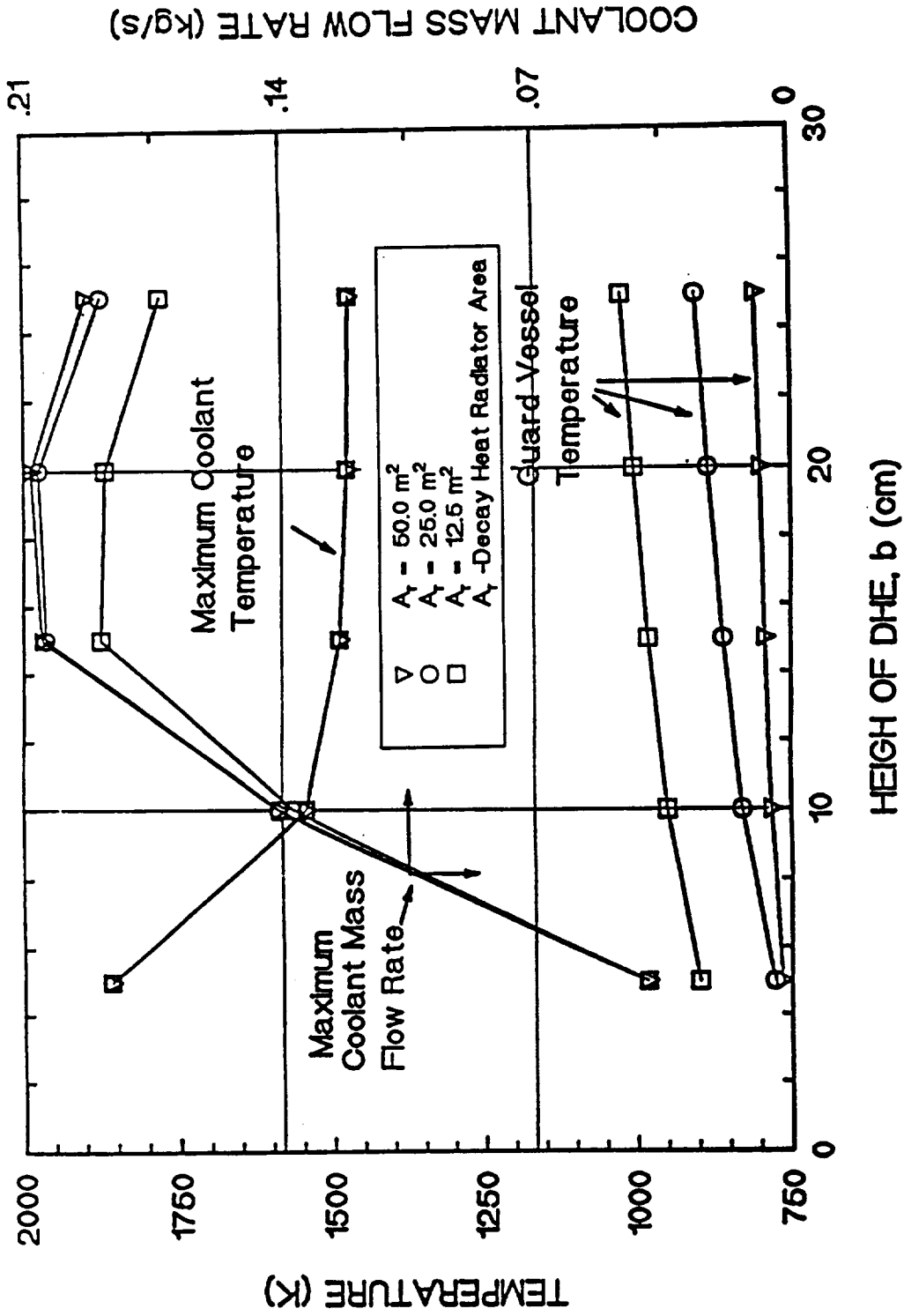
Fig. 23   Effect of Dimensions of the DHE Duct on the Coolability of the SP-100 Reactor after Shutdown.

55

Results show that even if the DHE duct height is doubled, the maximum coolant temperature after shutdown will still be more than 100 K higher than its nominal, full power operation value.

Figure (23) also indicates that increasing the surface area of the decay heat radiator on the lunar surface has no effect on the maximum coolant temperature, but reduces the radiator temperature, and, to a less extent, the coolant flow rate in the DHRL.

5.2.2 Effect of Elevation of DHE and Diameter of DHRL Pipes

Figure (24) presents the results on the effects of changing the elevation of the DHE and/or the diameter of the rise and down pipes in the DHRL on the coolability of the SP-100 by natural circulation after shutdown. As this figure shows, increasing the elevation of the DHE or increasing the diameter of the pipes improves the decay heat removal capability of the DHRL. However, increasing the diameter of the rise and down pipes beyond 8.5 cm insignificantly affects the maximum coolant temperature in the DHRL. The results in Fig. (24) demonstrate that increasing the elevation of the DHE increases the circulation rate of the coolant, resulting in a relatively lower maximum coolant temperature in the DHRL after reactor shutdown. For example, for a pipe diameter of 8.5 cm, increasing the elevation of the DHE from 1.96 m to 2.94 m increases the coolant flow rate by about 24 % (from 0.125 to 0.155 kg/s), but lowers the maximum coolant temperature in the DHRL by only 36 K (from 1562 K to 1526 K). Therefore, increasing the elevation of the DHE to improve the decay heat removal capability of the DHRL is not recommended because of the added system mass and excavation requirement. Also, increasing the diameter of the rise/down pipes is not recommended since it will affect the reactor design and the secondary loop. Instead, increasing the the height of the DHE duct, as discussed in the previous section, could better enhance the coolability of the SP-100 reactor after shutdown by natural circulation.

56

5.2.3 Effects of Radiator Area and Guard Vessel Heat Pipe Diameter

Figures (25a) and (25b) show the effect of the surface area of the decay heat rejection radiator and the diameter of the guard vessel heat pipes on the guard vessel wall temperature and the maximum coolant temperature after reactor shutdown. Fig. (25a) shows the base case guard vessel heat pipe diameter of 2.54 cm, while Fig. (25b) is for a larger heat pipe diameter of 3.81 cm. As delineated in these figures, within the first 20 seconds after shut down, the maximum coolant temperature is independent on the radiator area and/or the diameter of the guard vessel heat pipes. However, at later times up to 200 seconds after shutdown, increasing the radiator area from 12.5 to 25 m², slightly lowers the maximum coolant temperature. Further increase in the decay heat rejection radiator to 50 m² does not affect the maximum coolant temperature, hence the coolability of the system. It can also be seen in these figures that at times longer than 200 seconds after shutdown, both the radiator area and the diameter of the guard vessel heat pipes insignificantly affects the coolant flow rate or the maximum coolant temperature.

Figures (25a) and (25b) also show that increasing the guard vessel heat pipe diameter does not affect the maximum coolant temperature, but reduces the guard vessel temperature and increases the time after shutdown, beyond which decay heat rejection is restricted by the sonic limit of the heat pipes (see Section 4.3). For a heat pipe diameter of 2.54 cm, the sonic limit is reached at 20 seconds and 110 seconds after shutdown for a radiator area of 25 m² and 12.5 m², respectively (see Fig. (25a)). For the largest radiator area of 50 m², the radiator temperature (equal to the guard vessel temperature) immediately after shutdown is already below the sonic limit of the guard vessel heat pipes (see Figs. (25a) and (25b)). When the heat pipe diameter in the guard vessel is increased from 2.54 cm to 3.81 cm, the time to reach the sonic limit increased to 45 seconds and 190 seconds for a radiator area of 25 m² and 12.5 m², respectively. Therefore, using a larger guard vessel heat pipe can defer the time for reaching the sonic limit for the same radiator area.
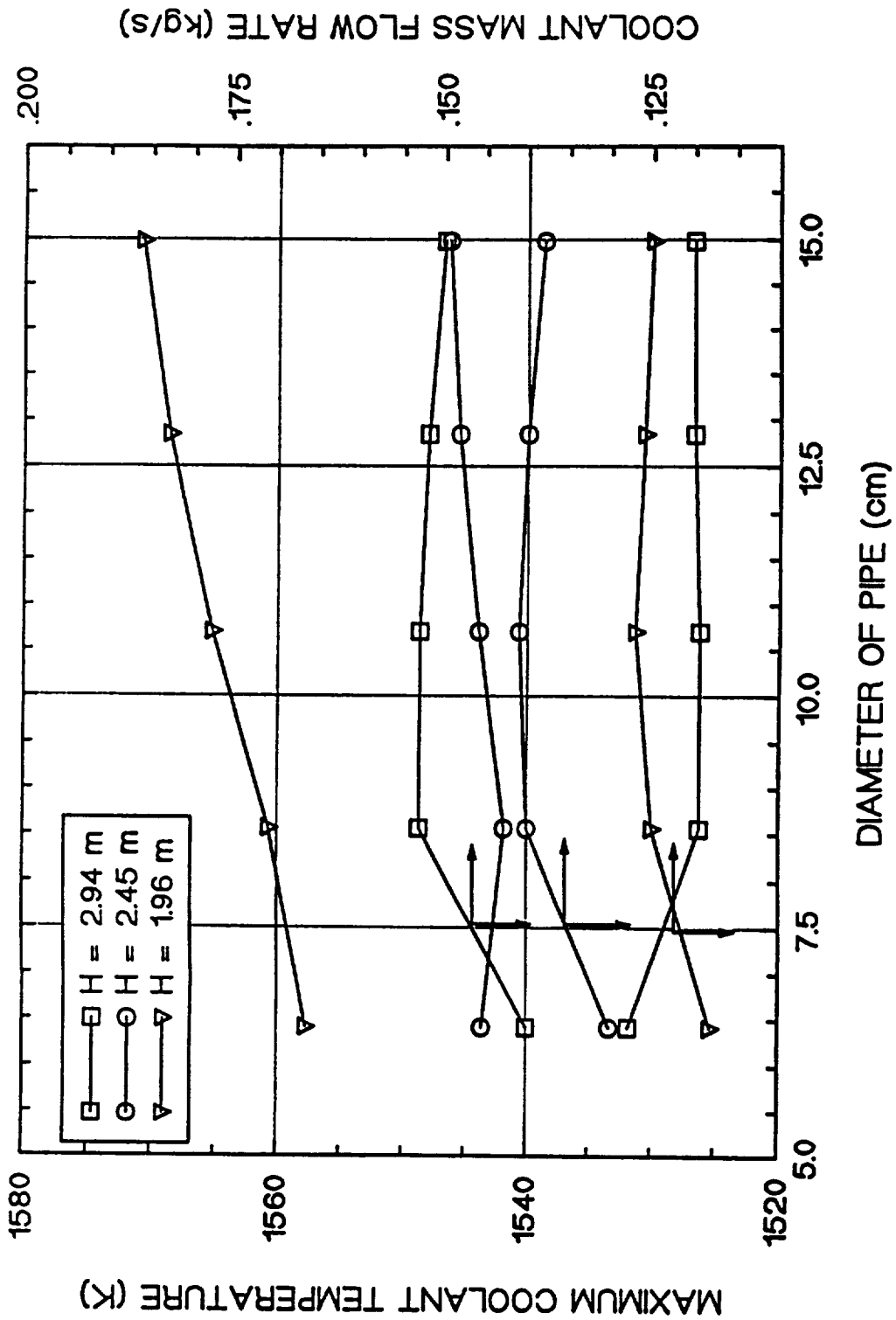
Fig. 24   Effect of Elevation of the DHE and Diameter of *Rise and Down Pipes* of the DHRL on   the Coolability of the SP-100 after Shutdown.

58

5.3 Effect of Gravity on the Decay Heat Removal

To identify the differences and similarities between test results at earth gravity and the actual system performance on the lunar surface, the effect of increasing the gravity constant from 1/6 g on the lunar surface to 1g on the thermal behavior of the DHRL was investigated. The results presented in Figs. (26)-(28) indicate that at earth gravity, the decay heat removal capability of the power system is significantly higher. As shown in Fig. (26), unlike on the lunar surface (see Fig. (20)), the maximum coolant temperature does not exceed its nominal value (at t=0). That means that in an earth-based preflight test, there will be no coolant overheat happening during natural circulation cooling after the reactor shutdown, even though this may happen on the lunar surface.

Figure (27) shows that the maximum coolant temperature in the DHRL at 1g, immediately after shutdown, is approximately 1380 K, which is about 140 K lower than its predicted value on the lunar surface. Moreover, the maximum fuel and cladding temperature could be as many as 50 K to 100 K lower than their values on the lunar surface (see Fig. (22)). Also, the maximum fuel temperature in the SP-100 reactor after shutdown would be lower, but the coolant flow rate would be higher than their values on the lunar surface. As Fig. (28) shows, the coolant flow rate by natural circulation in the DHRL during earth-based testing is more than twice that on the lunar surface. Furthermore, the frequency of the coolant flow oscillation on earth is higher than on the lunar surface, for the coolant mass flow rate on 1 g is higher.

These comparisons show that there is a large difference between the thermal behavior of the system after the reactor shutdown at 1 g and on the lunar surface. Recognizing these differences, an earth-based preflight test results could be used to predict the actual system performance on the lunar surface.
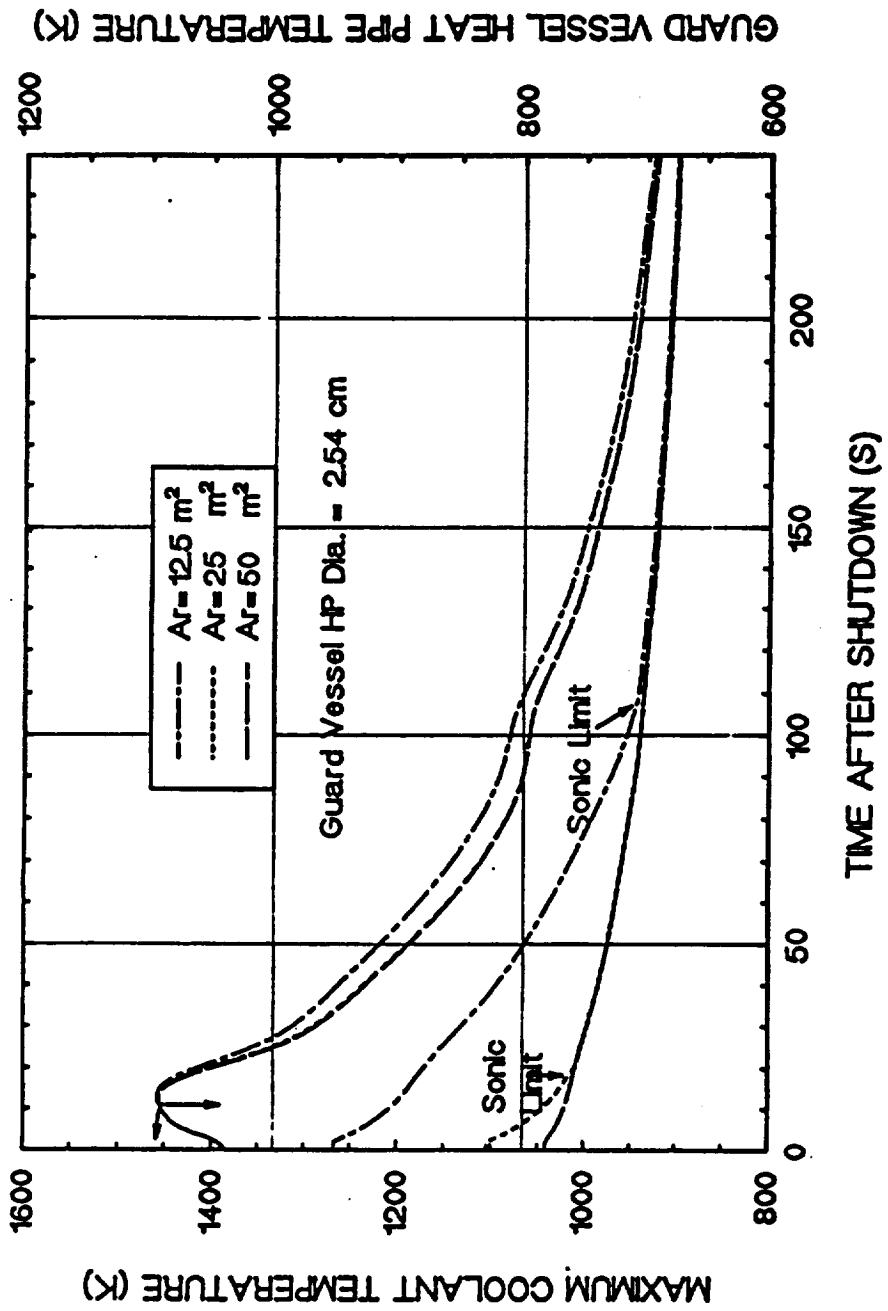
Fig. 25a   Calculated guard vessel and maximum coolant temperatures for diameter d=2.54 cm guard vessel HP and radiator area.
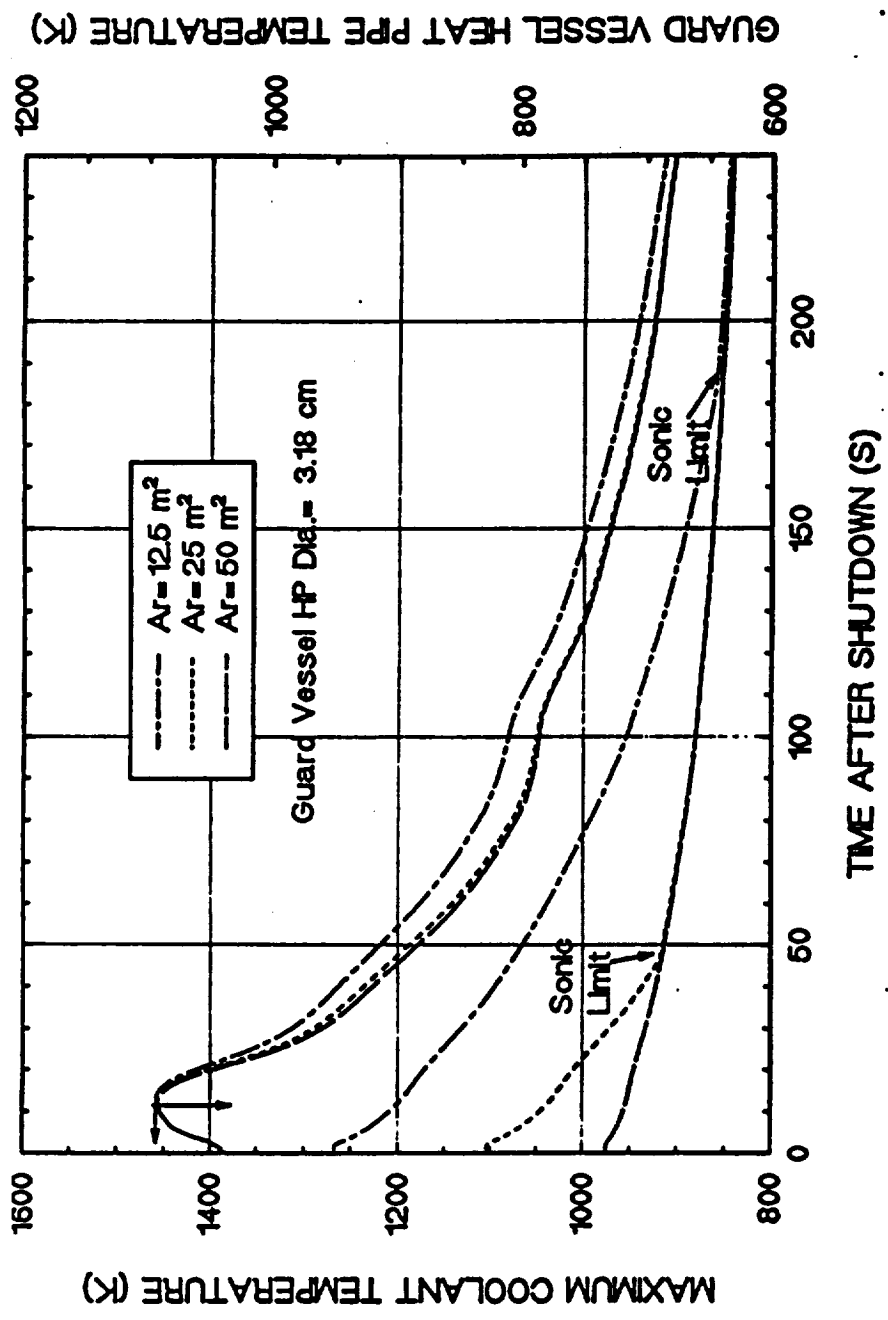
60

Fig. 25b   Calculated guard vessel and maximum coolant temperatures for
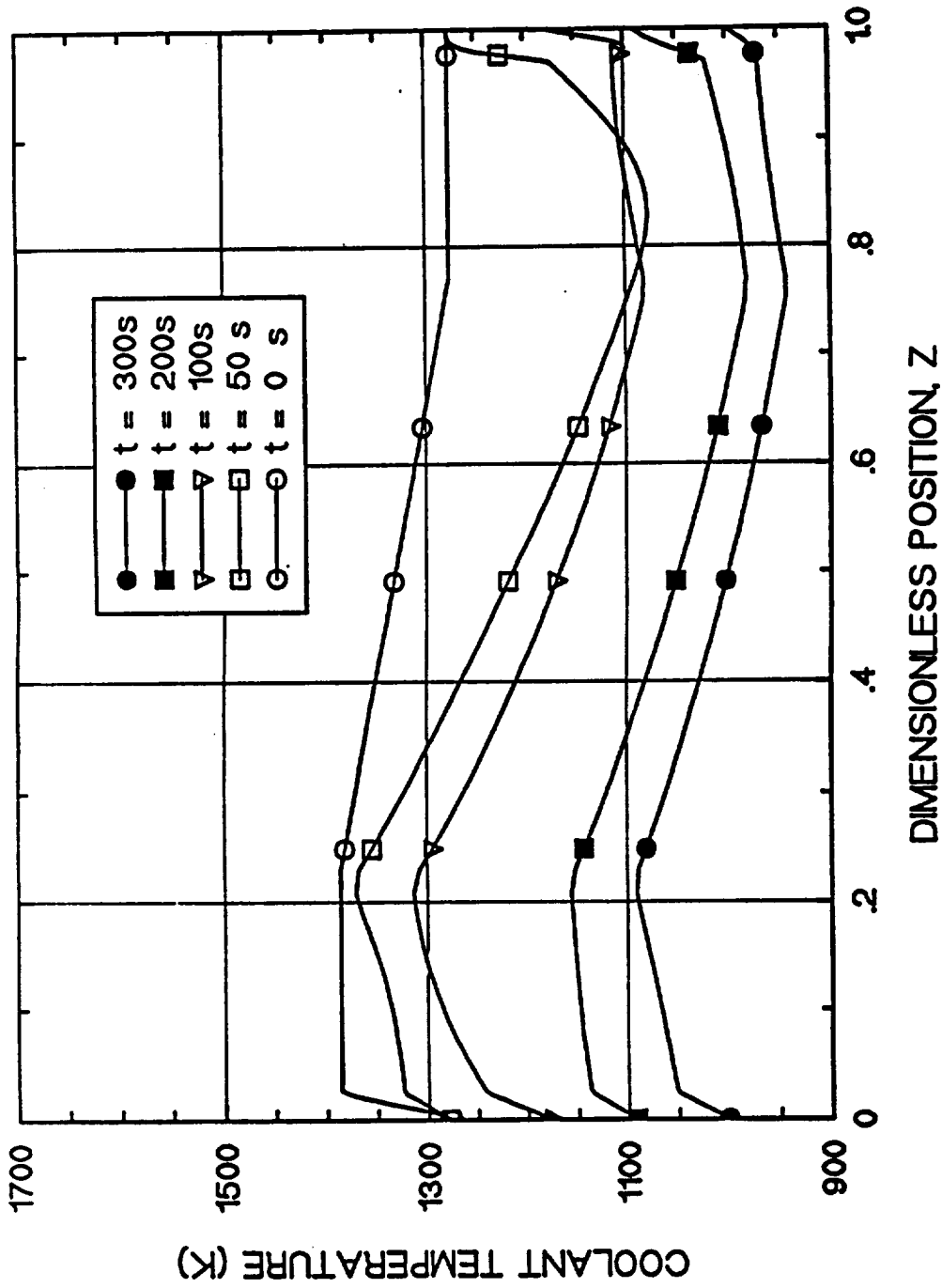diameter d=3.81 cm guard vessel HP and radiator area.

61

Fig. 26   Calculated Spatial Distribution of the Coolant Temperature in the DHRL at 1g.

62

6. SUMMARY AND CONCLUSIONS

The decay heat removal from an SP-100 reactor of a 550 kWe power system for a lunar outpost by natural circulation of lithium coolant was investigated. A transient model, which simulates the DHRL of the power system and incorporates axial conduction in the liquid metal coolant, has been developed and used to assess the system's decay heat removal capability. The effects of the surface area of the decay heat rejection radiator, dimensions of the DHE flow duct, elevation of the DHE, guard vessel heat pipes diameter, diameter of DHRL pipes, and gravity on the decay heat removal capability were examined.

Results showed that natural circulation of the lithium coolant in the DHRL would maintain the SP-100 reactor core safely coolable after shutdown. However, the lithium coolant in the adiabatic rise pipe, directly downstream of the reactor core, could overheat by as much as 175 K above its nominal operation value of 1355 K at approximately 200 seconds after shutdown. Such a coolant temperature overheat, which lasted for a very short time, can be reduced by as much as 50 K by increasing the height of the DHE duct up to 15 cm. A further increase in the DHE duct height, would have little effect on the decay heat removal from the SP-100 reactor core after shutdown. Increasing the elevation of the DHE slightly improves the decay heat removal capability of the DHRL, but does not justify the additional system mass and excavation on the lunar surface. Therefore, increasing the elevation of the DHE is not recommended since it does not significantly improve the system's decay heat removal coolability. It would strongly impact the mass and size of the system, and hence the excavation and launch costs.

Increasing the area of the decay heat radiator insignificantly affects the coolability of the DHRL; a radiator area in the order of 10-15 m^2, will be sufficient to maintain long term coolability of the power system by natural circulation. Analysis demonstrated that increasing the diameter of the heat pipes in the guard vessel does not influence the coolability of DHRL, it lowers the guard vessel wall temperature. Increasing the diameter of DHRL pipes up to a value of 8.5 cm insignificantly affects the coolability of the system, and therefore it is not recommended.

63

Results also showed that the thermal performance of the power system after reactor shutdown in an earth-based preflight test would be significantly different than that on the lunar surface. The maximum coolant temperature in the DHRL and the maximum fuel temperature in the reactor core could be as much as 140 K and 50 - 100 K lower than their values on the lunar surface. These results would be useful for relating data earth-based tests results to the decay heat removal capability of the actual power system on the lunar surface.
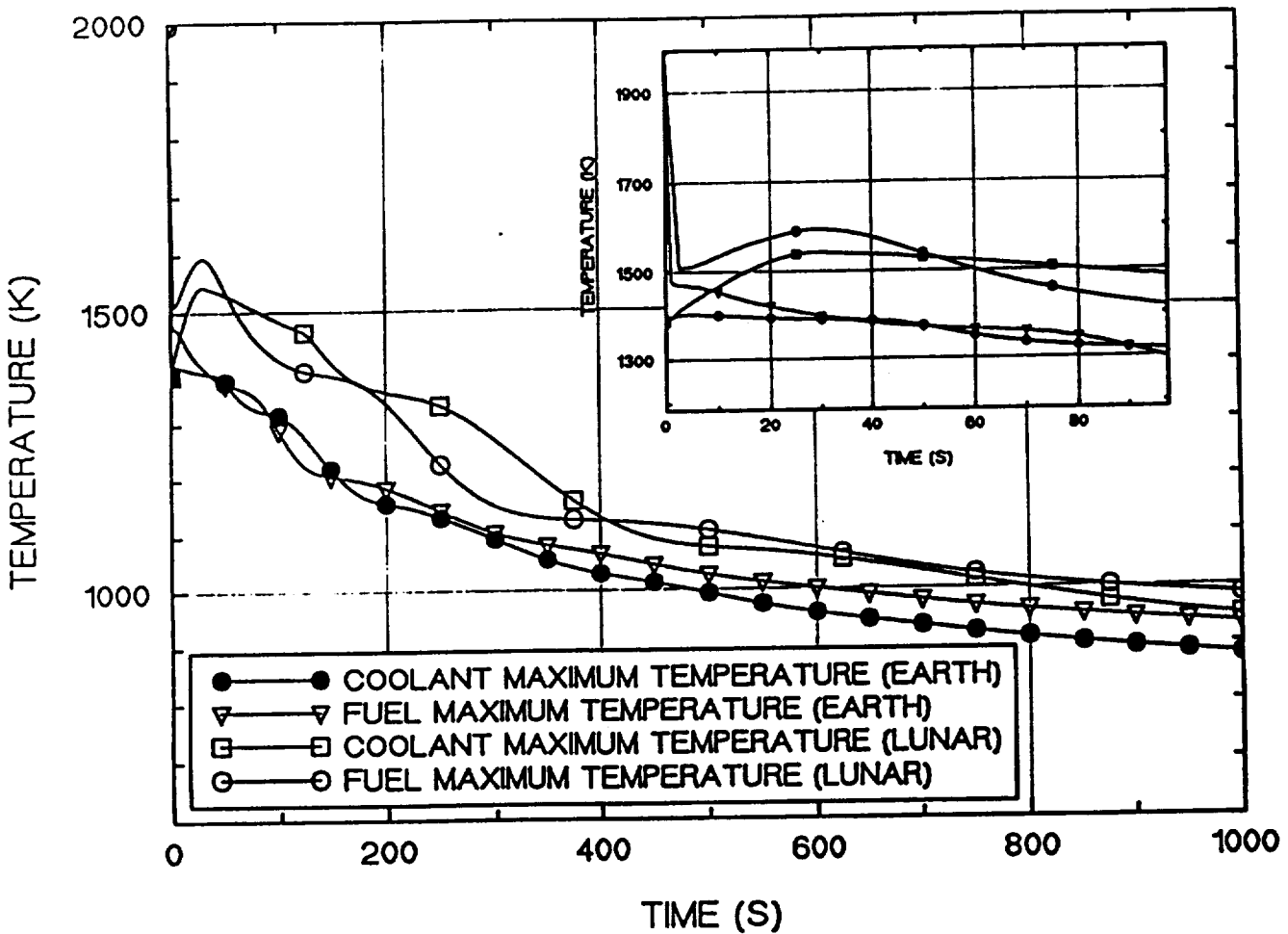

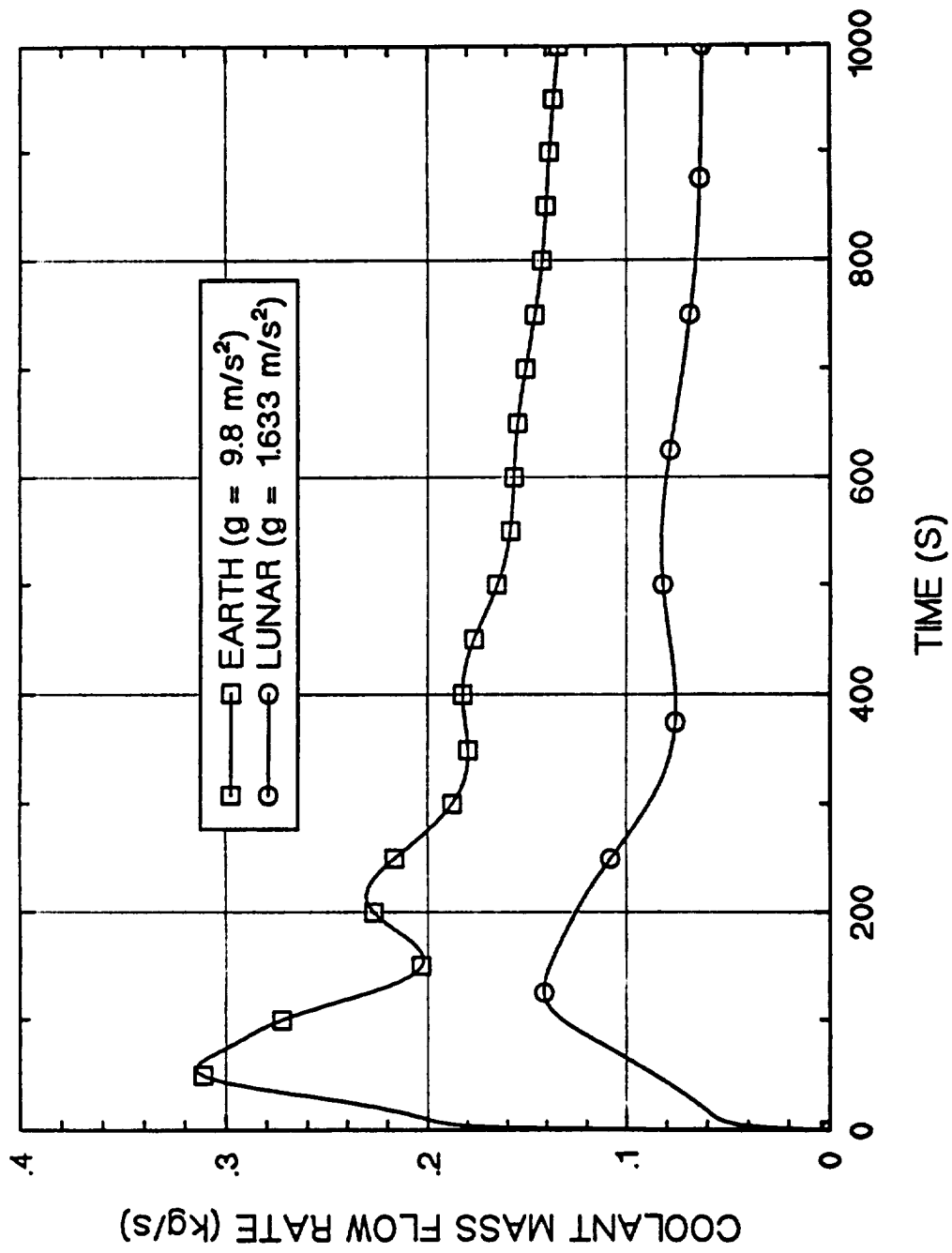Fig. 27   Effect of Gravity on Calculated Maximum Coolant and Fuel Temperatures after Reactor Shutdown.

Fig. 28   Effect of Gravity on the Coolant Mass Flow Rate in the DHRL after Reactor Shutdown.

65

Table 1. **Base Case Parameters for an SP-100,500-kWe Power System for a Lunar Outpost.**

Parameter	Value
1. EXTERNAL PIPES AND DHE	
Pipe height (m)	2.45
Pipe inner diameter (m)	0.107
Aspect ratio of DHE duct	0.26
Height of DHE duct (m)	10.0
Diameter of DHE circle (m)	2.07
Pipes wall thickness (m)	0.005
DHE Na heat pipe length (m)	0.3
Number of DHE Na heat pipes	100
Diameter of guard vessel heat pipes (m)	2.75
Pipe wall material	Nb-1% Zr
DHE pipe surface emissivity	0.8
2. GUARD VESSEL AND DECAY HEAT RADIATOR	
Guard vessel height (m)	3.53
Guard vessel inner diameter (m)	2.30
Number of guard vessel heat pipes	45
DHE/guard vessel radiation view factor	1.0
Emissivity of DHE surface	0.8
Emissivity of guard vessel wall	0.8
Radiator surface area (m^2)	25
3. REACTOR CORE	
Effective core height (m)	0.3175
Height of core vessel (m)	0.4258
Reactor core effective radius (m)	0.1764
Effective inner radius of core vessel (m)	0.2546
Total no. of fuel elements	1296
Fuel rod radius (m)	0.0037
Fuel rod lattice	triangular
Pitch-to-diameter ratio (P/D)	1.07
Fuel-cladding gap size (mm)	0.13
Cladding material	Nb-1% Zr
Fuel material	UN
Diameter of wire wrap (mm)	0.0548
Coolant type	Lithium
4. OPERATION PARAMETERS BEFORE SHUTDOWN	
Reactor thermal power (MW)	2.3
Core inlet coolant temperature (K)	1260
Core exit coolant temperature (K)	1355
Core coolant mass flow rate (kg/s)	14.1

APPENDIX A

Estimation of the DHE/Guard Vessel View Factor

The view factor between DHE and guard vessel was calculated according the geometries and dimensions of these two components. After simplification, the configuration of DHE/guard vessel is shown in Fig. (A-1). The DHE is a circular ring identified by 'L' in Fig. (A-1). The guard vessel is a hollow right column identified by '3' in Fig. (A-1). According to reference 6, the view factor between the DHE and Guard Vessel, F_{1-3}, is calculated by:

$$F_{1-3} = \frac{1}{L} [L + bF(b) + cF(c) - (L + b) F(L+b) - (L + c) F(L+c)], \qquad (A-1)$$

where:

$$F(x) = \frac{1}{2\pi} \left\{ \cos^{-1}\left(\frac{x^2-R^2+r^2}{x^2+R^2+r^2}\right) - \frac{r}{2l} \left[\left(\frac{(L^2+R^2+r^2)^2}{r^4} - 4(\frac{R}{r})^2\right)^{1/2} \right. \right.$$

$$\left. \left. \cos^{-1}\left(\frac{r(L^2-R^2+r^2)}{R(L^2+R^2+r^2)}\right) + \left(\frac{L^2-R^2+r^2}{r^2}\right) \sin^{-1}(\frac{r}{R}) - \frac{\pi}{2}\left(\frac{L^2+R^2-r^2}{r^2}\right) \right] \right\} \qquad (A-2)$$

b, c, L, r and R are defined in Fig. (A-1).

In our calculation, the DHE is discretized into some small segments. In the jth segment as shown in Fig. (A-1), the radiation view factor with the guard vessel, F_{j-3}, should be equal to the view factor between the DHE and guard vessel, F_{1-3}: i.e.

$$F_{1-3} = F_{j-3}.$$

67
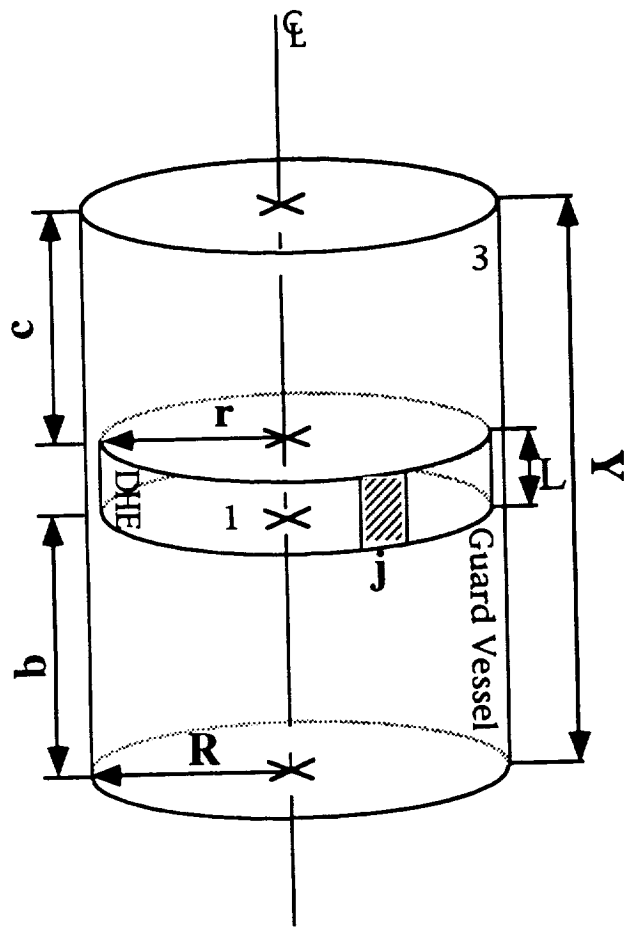
Fig. (A-1)   Configuration of DHE/guard vessel.

By the definition of view factor:

$$A_1 F_{1-3} = A_3 F_{3-1},$$ (A-3)

where A_1 and A_3 are the surface area the DHE and guard vessel respectively. For jth segment, also by definition:

$$A_3 F_{3-j} = A_j F_{j-3},$$ (A-4)

and

$$F_{3-1} = \sum_j F_{3-j}$$ (A-5)

Substituting Eqs. (A-4) and (A-5) into Eq. (A-3) yields:

$$A_1 F_{1-3} = \sum_j A_j F_{j-3}$$ (A-6)

Because

$$A_1 = \sum_j A_j$$

and F_{j-3} is a constant for a circular DHE,

$$F_{1-3} = F_{j-3}.$$ (A-6)

APPENDIX B

Momentum Balance Equation for DHRL

For the flow channel shown in Fig. (B-1), a control volumn, R, is selected. Assume that between time, t, and time, t+Δt, this control volumn changes from R= R_1 + R_2 to R'= R_2 + R_3, causing the fluid momentum to change from $\vec{M}_R = \vec{M}_{R1} + \vec{M}_{R2}$ to $\vec{M}_{R'} = \vec{M}_{R2'} + \vec{M}_{R3}$, where the vector $\vec{M}_{R2'}$ and $\vec{M}_{R2}$ represent the fluid momentum in the control volumn R2 at t+Δt, and t, respectively. Therefore, during the interval Δt, the rate of change of the fluid momentum can be expressed as:

$$\frac{\Delta \vec{M}_R}{\Delta t} = \frac{\vec{M}_{R'} - \vec{M}_R}{\Delta t} = \frac{\vec{M}_{R2'} - \vec{M}_{R2}}{\Delta t} + \frac{\vec{M}_{R3} - \vec{M}_{R1}}{\Delta t} , \qquad (B-1)$$

The first term on the RHS of Eq. (B-1) is the momentum change in R2; as $\Delta t \to 0$, S' $\to$ S and R' $\to$ R(see Fig. (B-1)), this term can be expressed as:

$$\lim_{\Delta t \to 0} \frac{\vec{M}_{R2'} - \vec{M}_{R2}}{\Delta t} = \frac{d}{dt} \int_R \rho_R \vec{V} \, dR , \qquad (B-2)$$

where ρ_R is the fluid density, $\vec{V}$ is its velocity vector in the control volumn R.

Similarly, the second term on the RHS of Eq. (B-1), which is the momentum change between volumn R_1 and R_3, can be expressed as:

$$\lim_{\Delta t \to 0} \frac{\vec{M}_{R3} - \vec{M}_{R1}}{\Delta t} = \int_s \vec{V}_s \, d\dot{m} , \qquad (B-3)$$

70
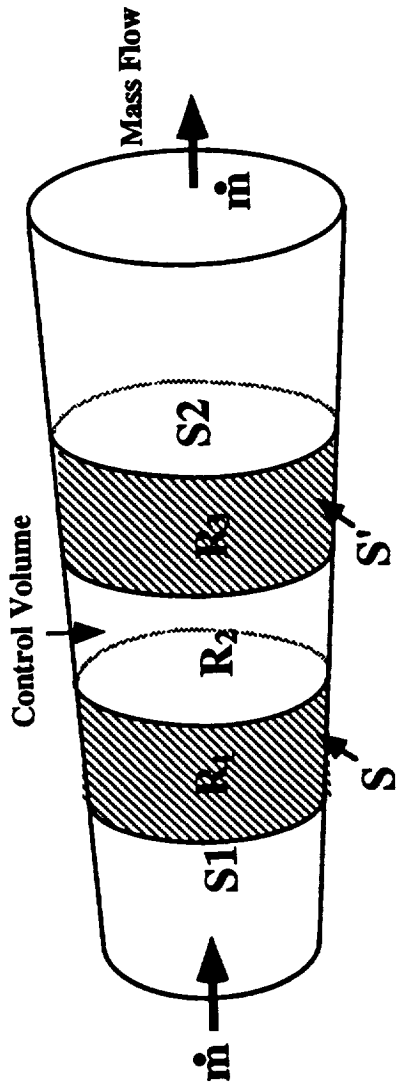
S   Surface Area of the Control Volume in t

S'   Surface Area of the Control Volume in t + Δt

Fig. (B-1).   Flow Channel for Momentum Balance.

71

where $\overrightarrow{V_S}$ is the fluid velocity vector at the surface S. The mass flow rate in the control volumn, R, can be expressed as:

$$\dot{m} = \rho_S \overrightarrow{V_S} \cdot \overrightarrow{dS},$$ (B-4)

Substituting Eq. (B-4) in to Eq. (B-3) and rearranging the result, yields:

$$\lim_{\Delta t \to 0} \frac{\overrightarrow{M_{R3}} - \overrightarrow{M_{R1}}}{\Delta t} = \int_S \left(\rho_S \overrightarrow{V_S} \right) \overrightarrow{V_S} \cdot \overrightarrow{dS},$$ (B-5)

From the Newton law, the total force acting on the control volumn, $\overrightarrow{F}$, is equal to the rate of change in momentum within the control volumn:

$$\overrightarrow{F} = \frac{d}{dt} \int_R \rho_R \overrightarrow{V} \, dR + \int_S \left(\rho_S \overrightarrow{V_S} \right) \overrightarrow{V_S} \cdot \overrightarrow{dS}.$$ (B-6)

For one-dimensional slug flow (i.e. the $\overrightarrow{V_S}$ is uniform at the inlet (S1) and outlet (S2) surfaces of the control volumn), the second term of Eq. (B-6) can be simplified as:

$$\int_S \left(\rho_S \overrightarrow{V_S} \right) \overrightarrow{V_S} \cdot \overrightarrow{dS} = \int_{S1}^{S2} \overrightarrow{V_S} \cdot \dot{dm} = \dot{m_2} \overrightarrow{V_2} - \dot{m_1} \overrightarrow{V_1},$$ (B-7)

Substituting Eq. (B-7) intoto Eq. (B-6), the one-dimensional flow momentum equation is:

$$\overrightarrow{F} = \frac{d}{dt} (M\overrightarrow{V}) + \dot{m_2} \overrightarrow{V_2} - \dot{m_1} \overrightarrow{V_1}.$$ (B-8)

72

Through the use of flow continuity ($\dot{m}_2 = \dot{m}_1 = \dot{m}$) and substitute the mass of the control volume $M = \rho \, \Delta V$, and the total force, $\vec{F} = \sum_i F_i$, Eq. (B-8) can be presented as:

$$\Delta V \frac{d}{dt}(\rho V) = \sum_i F_i - \dot{m}(V_2 - V_1) \tag{B-9}$$

The DHRL, shown in Fig. (B-2), was modeled using Eq. (B-9) The whole loop was divided into N segments and the energy balance equation wassolving in each segment (see Section 4.2.2). In the ith segment, except those located at the interface between different sections in the loop, Eq. (B-9) can be presented as:

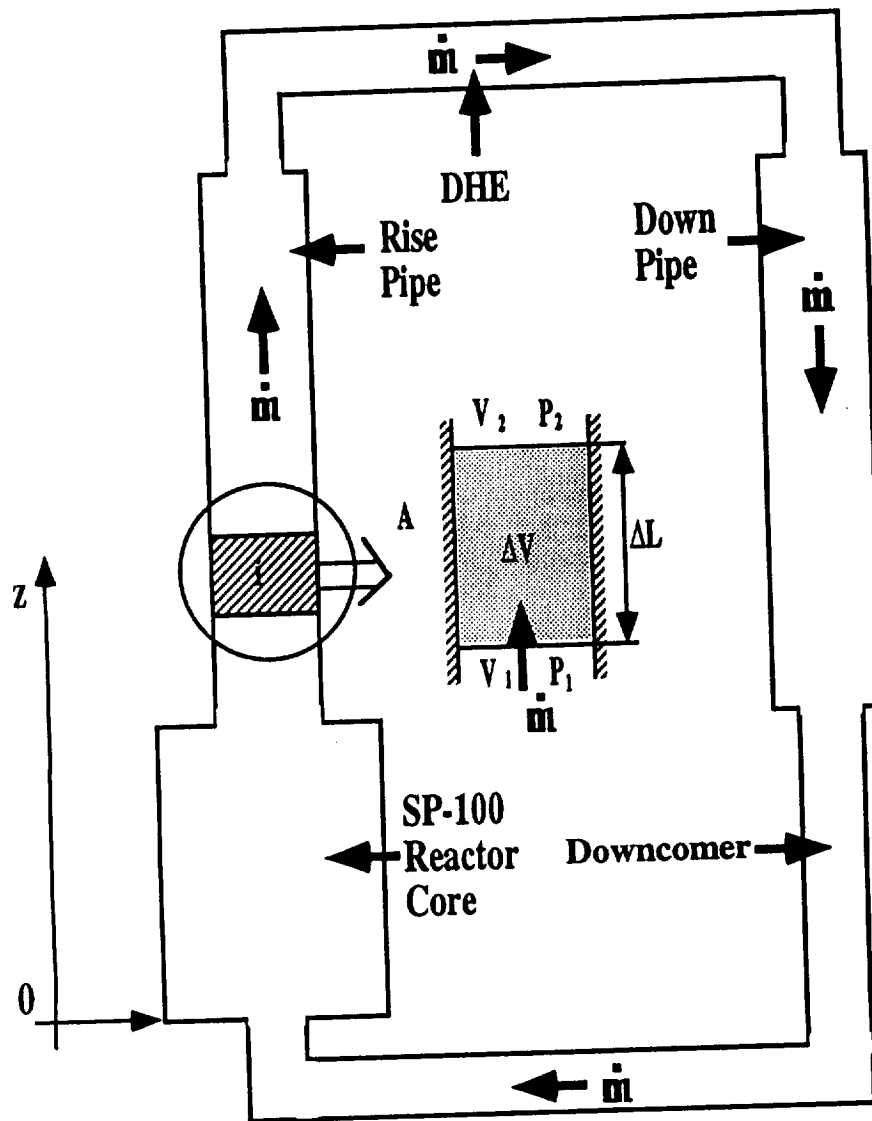$$\frac{\Delta V}{A} \frac{d}{dt}(\rho V A) = \sum_i F_i - \dot{m}(V_2 - V_1) \tag{B-10}$$

where A is the cross section area of the DHRL. The force balance in the loop is expressed as:

$$\sum_i F_i = \pm \Delta V \rho g + P_2 A_2 - P_1 A_1 - \Delta P_{fric} A \tag{B-11}$$

Substituting Eq. (B-11) into Eq. (B-10) and, $\Delta V = A \, \Delta L$, yields:

$$\Delta L \frac{d}{dt}(\dot{m}) = \pm A \rho g \Delta L + P_2 A_2 - P_1 A_1 - \dot{m}(V_2 - V_1) - \Delta P_{fric} A \tag{B-12}$$

Because A is not the same in the different sections of the DHRL, Eq. (B-12) was integrated over the whole DHRL as follow:

73

A   : Surface Area of the Segment
ΔV : Volume of the Segment
P   : Pressure
V   : Coolant Speed

Fig. (B-2). A Simplified Schematic of the DHRL.

74

$$\int_L \frac{d}{dt}(\dot{m})\ dz = \int_L \rho g A(z) dz + \int_L dPA(z) - \int_L A(z)\ dP_{fric} + \int_L \dot{m}\ dV(z)$$

<div align="right">(B-13)</div>

where L is the length of the DHRL. Since for the whole loop,

$$\int_L d(PA(z)) = 0 \quad \text{and} \quad \int_L \dot{m}\ dV(z) = 0 \quad ,$$

then the overall momentum balance can be written as:

$$\int_L \frac{d}{dt}(\dot{m})\ dz = \int_L \rho g A(z) dz - \int_L A(z)\ dP_{fric} \quad ,$$

<div align="right">(B-14)</div>

which is the same equation as Eq. (34) in Section 4.2.3.

REFERENCES

1. NASA, *Report of the 90-Day Study on Human Exploration of the Moon and Mars*, National Aeronautics and Space Administration (November 1989).

2. Bennett, G. L., and A. D. Schnyer, "NASA Mission Planning for Space Nuclear Power," *Proc. of the 8th Symposium on Space Nuclear Power Systems*, (Eds. M. S. El-Genk and M. D. Hoover), American Institute of Physics, New York, Vol. 1, pp. 77-83 (January 1991).

3. Truscello, V. C. and L. L. Rutger, " SP-100 Power System," *Proc. of the 9th Symposium on Space Nuclear Power Systems*, (Eds. M. S. El-Genk and M. D. Hoover), American Institute of Physics, New York, Vol. 1, pp. 1-24, (January 1992).

4. Harty, R. B., R. E. Durand, and L. S. Mason, "Lunar Electrical Power System Utilizing the SP-100 Reactor Coupled to Dynamic Conversion Systems," *AIAA/NASA/OAI Conference on Advanced SEI Technologies, Paper No. AIAA 91-3520*, Cleveland, OH (September 1991).

5. El-Genk, M. S. and H. Xue," An Investigation of Natural Circulation Decay Heat Removal from an SP-100 Reactor System for a Lunar Outpost", *Proc. of the 9th Symposium on Space Nuclear Power Systems*, (Eds. M. S. El-Genk and M. D. Hoover), American Institute of Physics, New York, Vol. 2, pp. 787 (January 1992).

6. Rea, S. N., "Rapid Method for Determining Concentric Cylinder Radiation View Factors," *AIAA Journal*, 13, 8 (August, 1975).

7. El-Genk, M. S. and J. T. Seo, " SNPSAM-Space Nuclear Power System Analysis Model," *Space Nuclear Power Systems 1986*, (Eds. M. S. El-Genk and M. D. Hoover) Orbit Book Company, Inc., Malabar, FL, 5, 111 (1986).

76

8. Jackson, C. B., et al., *Liquid Metal Handbook*, Atomic Energy Commission, Dept. of Navy, Washington, D.C. (July, 1955).

9. El-Genk, M. S. and J. T. Seo, " Parametric Analysis of the SP-100 System Performance," *Space Nuclear Power Systems 1987* (Eds. M.S. El-Genk and M. D. Hoover) Orbit Book Company, Inc., Malabar, FL, 7, 399 (1987).

10. Marr, D. R. and W. L. Bunch, "FTR Fission Product Decay Heat", HEDL-TIME 71-27, Hanford Engineering Development Laboratory (February 1971).

11. Harnett, J. P. and T. F. Irvine Jr., "Nusselt Values for Estimating Turbulent Liquid Metal Heat Transfer in Noncircular Ducts," *A.I.Ch.E. Journal* 3, 313 (1957).

12. Patankar, S. V., *Numerical Heat Transfer and Fluid Flow*, Hemisphere Publishing Corporation, NY (1980).

13. Chui, C. , W. M. Rohsenow, and N. E. Todreas, *Flow Split Model for LMFBR Wire Wrapped Assemblies*, Coo-2245-56TR, MIT, Cambridge, MA (1978).

14. El-Genk, M. S., J. J. Buksa, and J. T. Seo, " Decay Heat Thermal Management of an SP-100 System," *Space Nuclear Power Systems 1987* (Eds. M. El-Genk and M. D. Hoover) Orbit Book Company, Inc., Malabar, FL., 6, 99 (1987).

15. McGhee, J., M. S. El-Genk, and R. Rothrock, " An Assessment of the Helium Gas Behavior in SP-100 Class Reactors," *Proceedings of the 24th IECEC meeting*, 2, Paper # 899243, 1231 (August 6-11, 1989).

16. Yang, J. Y. and M. S. El-Genk, " Nucleation of Helium Gas Bubbles During the Cooldown and Freeze of Lithium Coolant in SP-100 Type Systems," *Proc. of 8th Symposium on Space Nuclear Power Systems*, (Eds. M. S. El-Genk and M. D. Hoover), American Institute of Physics, New York, Vol. 3, 1244 (January 1991).